DEVELOPMENT OF A TORQUE-CONTROLLABLE LOWER EXTREMITY EXOSKELETON FOR CRUTCH-FREE 3D WALKING SUPPORT

A Thesis

by

Mehmet Can YILDIRIM

Submitted to the
Graduate School of Sciences and Engineering
In Partial Fulfillment of the Requirements for
the Degree of

Master of Science

in the
Mechanical Engineering

Özyeğin University
December 2018

DEVELOPMENT OF A TORQUE-CONTROLLABLE LOWER EXTREMITY EXOSKELETON FOR CRUTCH-FREE 3D WALKING SUPPORT

Approved by:

Assistant Professor Regaip Barkan Uğurlu, Advisor
Mechanical Engineering
Özyeğin University

Assistant Professor Evren Samur
Department of Mechanical Engineering
Boğaziçi University

Assistant Professor Polat Şendur, Co-Advisor
Mechanical Engineering
Özyeğin University

Assistant Professor Uğur Tümerdem
Department of Mechanical Engineering
Marmara University

Date Approved: 24 December 2018

Assistant Professor Ramazan Ünal
Mechanical Engineering
Özyeğin University

To my parents

ABSTRACT

Spinal cord paralysis is a condition, which is formed due to full or partial loss of sensorimotor and autonomous functionalities of the spinal cord. Paraplegia is a type of spinal cord injury which causes functionality loss in patients' lower bodies, even though their upper body is completely healthy. Active exoskeleton robots are the most practical approach to regenerate the walking function of paraplegic patients. In a fundamental way of this approach, patients wear a robotic system that can move their legs in the forward direction. Exoskeletons are wearable and powered robotic systems which enhance users mobility and endurance capabilities. The primary goal of this thesis study is to develop such an exoskeleton system which is capable of providing crutchless 3D walking support for those who suffer from paraplegia or similar pathological lower body conditions. During this thesis, an 8-DoF lower extremity exoskeleton is developed, and equipped with custom-made Series Elastic Actuator (SEA), for high fidelity torque control. Particularly developed SEA modules are designed to have high torque density, and this actuation unit is analysed, tested according to an integrated design approach.

ÖZETÇE

Omurilik felci, omurilikteki duyudevinimsel ve otonom fonksiyonların tamamen veyahut kısmen kaybı sonucu oluşmaktadır. Omurilik felcinin bir türü olan paraplejide hastalar üst vücutları tamamen sağlıklı olmasına karşın, alt vücutlarında tamamen fonksiyon kaybı yaşamaktadırlar. Bahsi geçen hastalarda yürüme işlevini tekrar oluşturmanın en pratik çözümü dış iskelet sistemleridir. Bu sistemlerin en temel uygulamalarında hastalar ileri adım atmalarını sağlayan robotik bir sistem giymektedirler. Dış iskeletler genel olarak giyen kullanıcının mobilite ve dayanıklılık seviyesini arttıran cihazlardır. Bu tezin temel amacı ek bir destek olmaksızın parapleji ve benzer rahatszlklar alt vücutta hareket sorunu çeken bireylere koltuk deyneği olmadan 3B yürüme desteği verebilecek bir dış iskelet sisteminin geliştirilmesidir. Tez süresince 8 serbestlik dereceli bir alt vücut dış iskelet sistemi geliştirilmiş olup, yüksek bağlılıklı tork kontrolü için özel geliştirilmiş Seri Elastik Eyleyiciler ile tahriklenmiş ve bu eyleyiciler entegre tasarım yaklaşımına göre analiz ve test edilmiştir.

ACKNOWLEDGEMENTS

First of all, I would like to thank Dr. Ugurlu, my thesis advisor, sincerely for giving me an opportunity to play all these resources, for his guidance and patience throughout this work (especially with my manuscripts). I would also like to thank Dr. Sendur, my co-advisor, for his guidance and his limitless help, without his inputs this thesis would not be at this point. I am also grateful/thankful to Dr. Bebek's for his continuous guidance since my freshman year.

I wish to thank my thesis committee members who were more than generous with their expertise and precious time. Thank you Dr. Samur, Dr. Tumerdem, and Dr. Unal for agreeing to be on my committee.

I want to thank these great people for their support; Talha Kansizoglu, Sinan Coruk, Sinan Emre, Mustafa Derman, Ulas Yildirim, Mehmet Polat Kuntuz, Onur Ersoy, Ayberk Bilgin, Umut Zeynep Uras, Onur Bilgin, and Ahmed Fahmy Soliman.

Special thanks to Baris Balci, Gorkem Muttalip Simsek, Kortan Berat Godekoglu, and Simge Kilic for their support and inspiration during this work , if it weren't for them I would not be able to succeed.

Works shown in this thesis are supported by the Scientific and Technological Research Council of Turkey (TUBITAK), with the project 215E138.

TABLE OF CONTENTS

LIST OF TABLES

LIST OF FIGURES

AF/D Ankle Flexion and Dorsiflexion

AI/E Ankle Inversion and Eversion

BCM Body Center of Mass

BFDCM Brushless Frameless Direct Current Motor

CAD Computer Aided Design

CNC Computer Numeric Control

CoEx Compliant Exoskeleton

CoM Center of Mass

DOF Degrees of Freedom

FEA Finite Element Analysis

F/D Flexion and Dorsiflexion

F/E Flexion And Extension

HA/A Hip Abduction And Adduction

HD Harmonic Drive

HF/E Hip Flexion And Extension

Humanoids IEEE-RAS International Conference on Humanoid Robots

ICRA IEEE-RAS International Conference on Robotics and Automation

IK Inverse Kinematics

I/E Inversion and Eversion

KF/E Knee Flexion And Extension

PEA	Parallel Elastic Actuator
SCI	Spinal Cord Injury
SEA	Series Elastic Actuator
SQP	Sequential Quadratic Programming
ToRK	Turkish Robotics Conference
TTM	Torsional Testing Machine
WEROB	The International Symposium on Wearable Robotics
WHO	World Health Organization
ZMP	Zero Moment Point
3D	Three Dimensional

CHAPTER I

INTRODUCTION

Spinal cord paralysis is a condition, which results form the full or partial loss of sensorimotor and autonomous functionalities of the spinal cord[2]. Various neurological diseases, car accidents, sports injuries, and falls are responsible for most of the cases in spinal cord functionality loss [3]. According to the World Health Organization (WHO) data [2], 250,000 to 500,000 people suffer from spinal cord paralysis which affect them in the form of inability to sense and move. Specifically for Turkey, approximately 150,000 patients are in similar conditions in accordance with the data from The Spinal Cord Paralytics Association of Turkey (2015). Being a highly traumatic disease, the negative effects of the spinal cord paralysis on the patients' life quality have been widely discussed in the literature [3–5].

In particular, the patients with a diagnosis of T1-T2 thoracic paraplegia experience functionality loss in their lower body even though their upper body is completely healthy. After a traumatic Spinal Cord Injury (SCI) one may need major health service in acute phase of the primary condition. However, afterwards same patient require only basic service and help, to maintain his health [6]. Such measures, treatment and assistance, should start as soon as possible and be made accessible as close as feasible to where individual with SCI live [7]. On the mobility side, being not able to walk is generally compensated with wheelchairs; however, there are health risks such that these patients may suffer from osteoporosis, calcification in the excretory system, spasticity, difficulties in digestion and excretion, and heterotopic ossification [6, 8]. Using a wheelchair also introduces some issues like pressure wound, bone and muscle tissue loss, and aches on arms and shoulders [9].

The issues caused by the walking disabilities are not only restricted with physiological ones. Wheelchairs that the patients utilize have certain condition impediments. These vehicles can only move on level and wide surfaces, which makes them vulnerable when the steps, stairs, and narrow pathways exist. In addition these problems, the paraplegic patients may need to adapt to mental issues [10, 11].

As mentioned in WHO Global Disability Action Plan for 2017-2021 [7], assistive methods are developing rapidly and adopts every possible previously developed system such as software, devices, technique regardless of whether it is procured industrially, adjusted or altered to enhance the utilitarian abilities of people with inability. Assistive innovations assume an enormous job in empowering individuals with disabilities to work and partake. For the paraplegic patients lives these advancements touched in order to eliminate the side effects robotic-based treatments were introduced [12]. First of them was a rehabilitation system, which is attached to the ceiling and called locomotor, that aims to regenerate the motor functions of the patient. This method is only suitable for patients that have muscle and joint deficiency. However, scientific research and data show that neither the full nor the partial paralysis can be treated using this approach [13, 14]. The reason behind this argument is that the characteristics of SCI are generally permanent.

The most practical approach to regenerate the walking function of paraplegic patients is active exoskeleton robots [12, 15]. In this approach, patients wear a robotic system that can move their legs in the forward direction. The first generation of these devices was able to support the patient actively from the hip and the knee Flexion And Extension (F/E) joints. The upper body is actively used to provide balance with crutches. Two major examples can be given as HAL and ReWalk [16, 17].

1.1 Literature Review

This study focuses on two main areas: **i)** development of a SEA and **ii)** development of a lower body exoskeleton. In this section, the literature on these areas are reviewed separately and provided in Section 1.1.1 and Section 1.1.2 respectively for the eoxkseleton and SEA.

1.1.1 Lower Body Exoskeleton State-of-the-art

Powered lower body exoskeletons are proven to be useful systems to help paraplegics regain walking ability [18]. The state-of-the-art lower body exoskeletons usually have two active Degrees of Freedom (DOF) at the knee and hip joints, along the F/E axis [17, 19–26]. Such a kinematic configuration can move the user's leg forward; however, it does not suffice for balancing or even standing still. Therefore, the user needs to involve her/his upper body via crutches to maintain static balance. Despite the fact that these robots do not help patients with 3D walking, they achieve to help patients recover from certain physiological and psychological difficulties which were mentioned in the Section 1. A notable decrease in pressure wound, better circulatory function and regaining the ability to walk are some benefits of using exoskeletons [15, 16, 27].

When patients use crutches or walkers to balance with an exoskeleton, it causes aches on arms and shoulder joints after long periods [28–31]. The expectation from the newer generation is to come up with better designs that will make the use of the additional artifacts to balance obsolete. In order to achieve self-balancing during robot-aided walking, it is required to increase the number of active DOFs. For example, an active ankle joint along the Flexion and Dorsiflexion (F/D) axis is necessary in sagital plane ballance [32, 33]. Moreover, the Three Dimensional (3D) walking motion dictates that the human BCM must be laterally swayed; therefore, a HA/A joint must be added as well [34, 35]. Following this strategy, a crutch-free walking support could be provided by the fully-actuated exoskeletons, which also include an

active AI/E (roll axis) joint [36, 37].

Increasing the number of active joints evidently helps the cause of self-sustained walking with the expense of increased overall weight. In particular, the high torque output requirement enforces engineers to make use of large motors with gear boxes, causing these systems to be relatively bulky. This may reduce the patient acceptance and may cause comparatively slow walking performance. While the literature suggests the use of minimum 8 DOF as enough for the 3D walking support, application of such systems are not frequent. Soliman et al. [38, 39] showed that 3D walking is possible with only 4 DOF per leg. As systems like [35] designed for such a combination, these systems requires additional DOF with some passivity for complete performance.

1.1.2 Series Elastic Actuators State-of-the-art

The type of actuators used in an exoskeleton design is an important design consideration. Exoskeleton robots are mostly designed with rigid actuators [17, 32, 34], which are controversial due to their suitability for physical robot-human interaction, safety, and physiological fitness criteria [16]. Torque control and physical elasticity traits are crucial in systems like exoskeleton robots, where a robot and a human work in physical contact [40–42]. Physical elasticity plays an important role when compensating the reaction forces from the environment [19]. Contemporary robotic systems are no longer experiment-only laboratory gadgets; rather, they are required to physically interact with humans in a safe manner [41], or to modify the outer environment to a human-like extent [43]. These enhanced interaction capabilities are directly linked to torque control, which stresses the importance of torque-controlled actuators [44].

The most simplistic, yet highly efficient form of torque-controlled actuation may be addressed by means of series elasticity, namely, series elastic actuators (SEAs) [45, 46]. SEAs are known to provide advanced control capabilities as they allow the synthesis of high fidelity torque control through the use of elastic elements that is

replaced between the motor and mechanical output [47]. Therefore, they are widely used in legged robots, rehabilitation robots and human-friendly robots [48–50].

Compliant actuation design may emerge in various forms [44]. To name a few, Veneman et al. devised a SEA mechanism with Bowden cables [50]. Van Ham et al. synthesized an actuator that has mechanically adjustable compliance [51]. Paine et al. designed a high-performance SEA mechanism that includes a piston-style ball screw and a concentric elastic element [52]. Sariyildiz et al. combined two springs with distinct stiffness values to achieve high-bandwidth motion control [53]. Rouse et al. devised a clutchable SEA unit to minimize energy consumption [54]. Tsagarakis et al. developed a SEA that was comprised of six optimally tuned linear springs for efficiency [55].

A SEA obeys the dynamics of a two-inertiae system, which has multiple vibration modes [56]. In particular, SEAs with lower stiffness may suffer from low motion control bandwidth and stability issues, despite their practical use in energy minimization [57]. To this end, one alternative method for SEA design is the use of custom-built torsional springs that are coupled with high-resolution encoders to achieve fine torque measurement in which torque resolution is below the respective cogging torque value [58–61].

An example of such a SEA is used in Robonaut-2, in which the NASA researchers built a custom spring topology [59]. Negrello et al. employed a torsional bar as the elastic element to ensure a linear stiffness profile [58]. Parmiggiani et al. made use of a curved beam structure, which allowed them to obtain an analytical model for the spring [60]. Accoto et al. coupled two identical custom torsional springs to achieve both torque and stiffness requirements [61].

In general, FEA based topology selection is adopted. These created topologies are then tested by using the actuator's dynamics or using an additional sensing unit. Such an approach is deemed proefical from design point of view, yet it cannot fully reveal it

the actuator is robust for long term repetitive use. In a different aspect, when a SEA reaches to an unexpected temperature, researchers used active cooling systems [62–64]. Even though all these suggested methods gave sufficient results [43, 59, 63, 65–69], no inclusive development scheme that covers all following issues was suggested; **i)** member wise experimental verification, **ii)** stiffness modelling under high-bandwidth varying frequencies, **iii)** thermal response of the system under a realistic working condition, **iv)** fatigue life, and finally **v)** force control quality.

1.2 Objectives of the Thesis

The literature highlights both the necessity and challenge of the current robotic solutions in the rehabilitation field. Two main challenges are **i)** insufficient actuation and **ii)** human-machine interaction. However, the literature also point out a solution to these problems; an exoskeleton with active joints just enough to attain 3D walking support and an interference capacity which allows the system to sense and be compliant to both human and the environment. By considering these two challenges, an under-actuated exoskeleton with force sensing capability is considered. By having two main objectives in mind:

i) 3D dynamic walking support: 3D walking support will be provided without the need of auxiliary tools such as crutches and upper body engagement.

ii) High power SEA: The robot will be powered via novel series elastic actuators with high torque-to-mass ratio to ensure dependable, safe and physiologically consistent human-robot interaction.

For these purposes, an exoskeleton with 8 active DOFs has been determined as the starting point. Furthermore, a spring-supported passive joint is also considered through simulation studies. SEA was selected for the actuation of these 8 active DOFs due to the requirement on the force sensing. Design process of the system

was initiated with the development of the proper SEA unit for the application, see Chapter 2. In addition, to that a possible spring-supported joints were investigated and a passive joint development framework was formed, this study is presented in Chapter 3. Finally, the design of the exoskeleton was accomplished in accordance with the design of the actuator, human parameters, and the locomotion strategy, see Chapter 4.

CHAPTER II

SERIES ELASTIC ACTUATOR DEVELOPMENT

The finalized SEA design is a result of a long-term research and an iterative development process. A detailed flow for the development procedure can be seen in Figure 1. Details on the design process will be explained in the consequent chapters.

In this chapter, respectively these topics will be covered; initial study done on the SEA, comprehensive design work on the SEA is given in Sections 2.1 to Section 2.5. Then brief results for the implemented controllers will be shared and finally in 2.6 final product of the development process CoEx-SEA-B v1.2 will be presented.

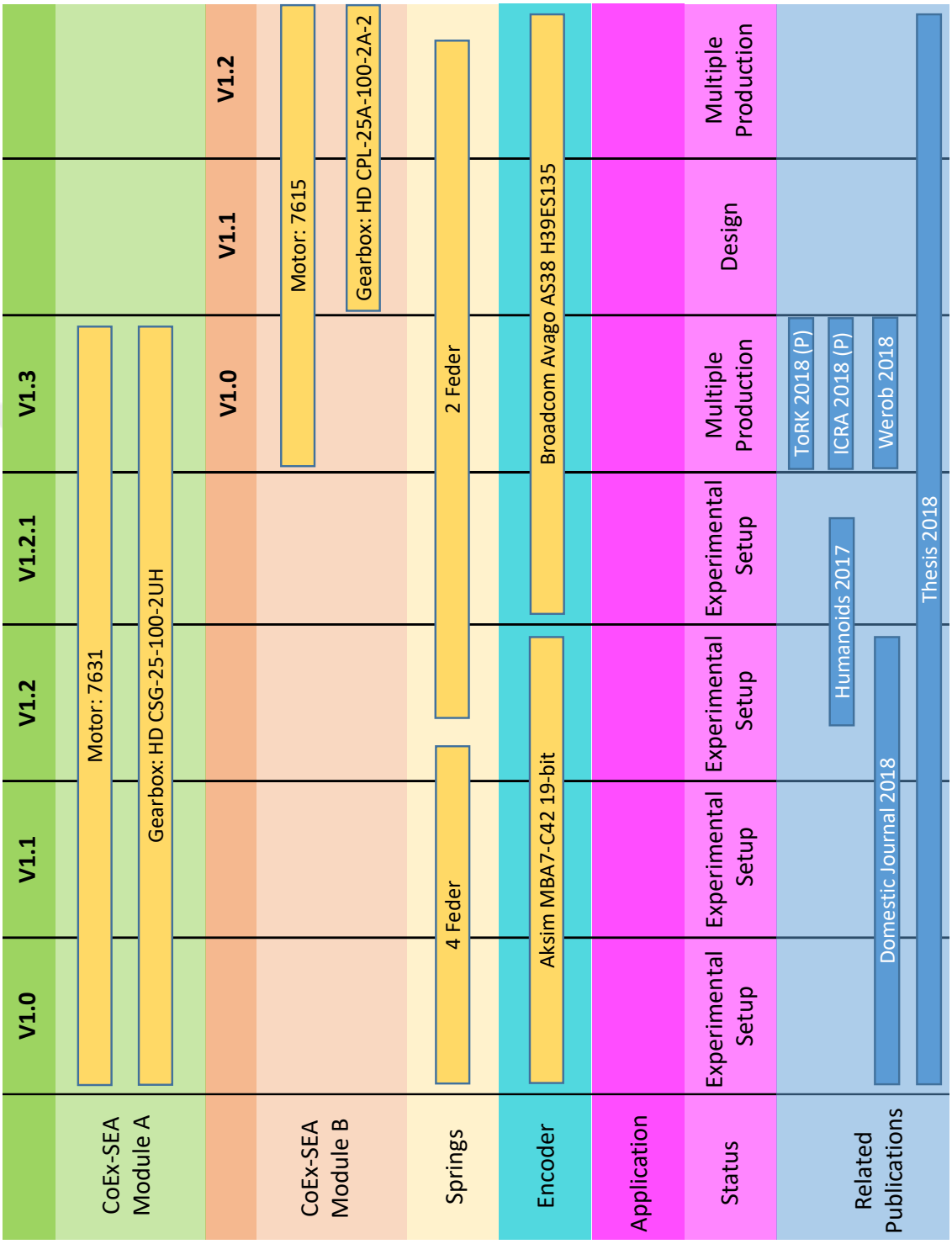

Figure 1: SEA timeline

2.1 Structural Design

Two distinct SEA units were developed, namely Compliant Exoskeleton-SEA A & B (CoEx-SEA). The developed SEA units consist of three major components: **i)** a frameless brushless DC motor (Kollmorgen TBMs-7615 & 7631), **ii)** a strain wave gear (Harmonic Drive (HD) CSG-25, 1:100 transformation ratio), and **iii)** a torsional spring that acts as a torque sensor. Detailed specifications of CoEx-SEA are listed in Table 1.

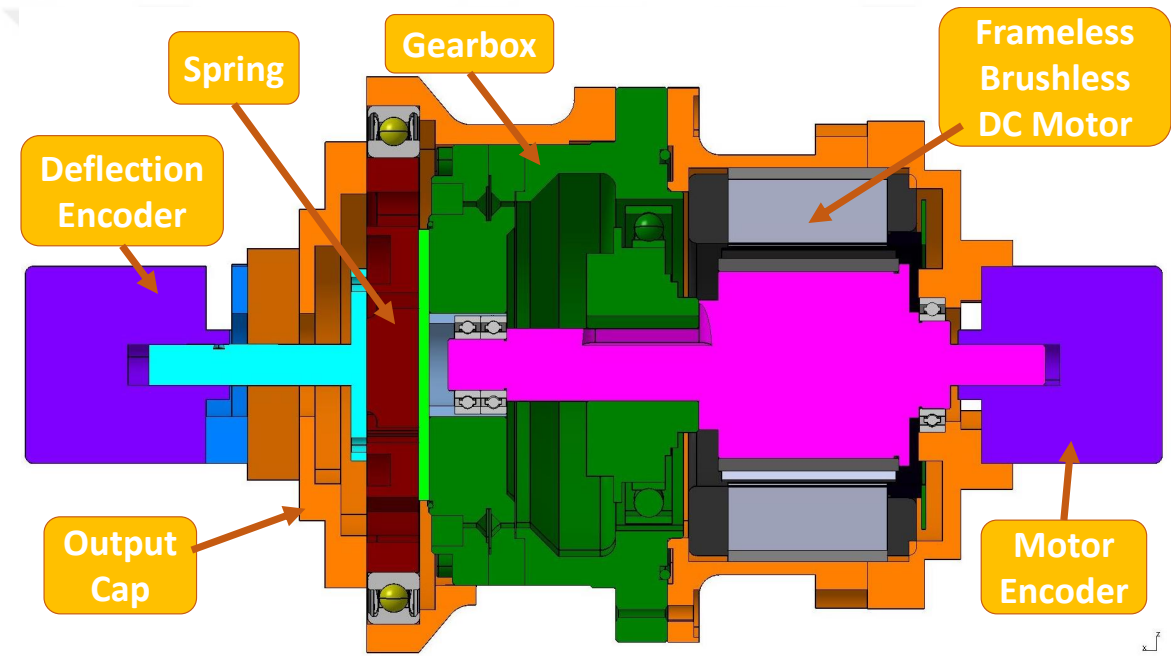

Figure 2: CAD model of the CoEx-SEA unit.

Table 1: The properties of SEA Module

Specification	CoEx-SEA (A)	CoEx-SEA (B)
Max. Angular Speed (rpm)	26.33	44.09
Max. Continuous Torque (Nm)	164	96
Mass (kg)	3.09	2.87
Dimensions (r x L) (mm x mm)	55.5 x 153	55.5 x 135
Stiffness (Nm/deg)	91	91
Torque Resolution (mNm)	3.90	3.90
Torque-to-mass Ratio (Nm/kg)	53.07	33.45
Cost (Euro)	$\approx$ 3700	$\approx$ 2900

The CAD model of CoEx-SEA is displayed in Fig. 2. The output of the HD is connected to the torsional spring at its center. The output cap of the unit and the input of the spring are connected to the outer circle of the spring. Two 23-Bit (Broadcom Avago AS38 H39ES135) encoders are integrated to measure motor angle and torsional deflection, respectively. It is argued that an encoder-based torque sensing is more advantageous than their load-cell based counterparts [70]. The actual SEA unit is displayed in Fig. 3.

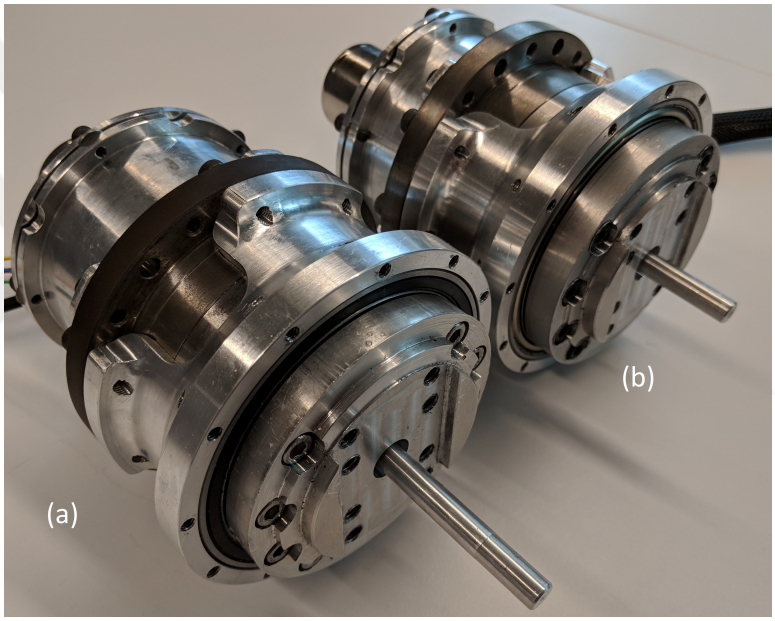

Figure 3: CoEx-SEA units (a) CoEx-SEA-A unit, (b) CoEx-SEA-B unit

2.2 Initial Design

At the initial stage of the development, combination for the HD and Brushless Frameless Direct Current Motor (BFDCM) was selected, in the next phases of the project all improvements were done on these selected systems. Meanwhile, some other components of the SEA and the HD were changed to address control issues and fundamental design requirements. Especially two main components must be highlighted in this part: **i)**encoder and **ii)**the elastic component; torsional spring.

For the design of the SEA, two rotary encoders are required. The first encoder

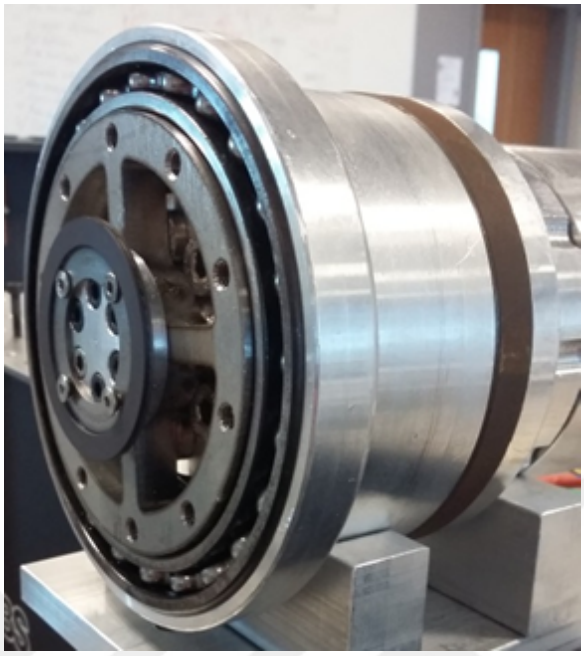

Figure 4: Initial Design with four-feder spring and an encoder ring

is used to measure the motor position. A second encoder is used for measuring the deflection angle of the spring. For size requirements, Aksim MBA7-C42 rotary encoders with 19-bit resolution are used. In the initial design, the motor is fixed to the rotary encoder frames, and only coarse adjustments could be made regarding the distance between the motor and the encoder cap. The distance specified by the manufacturer between the magnetic disc and the encoder chip is $0.1mm$. Due to the lack of proper installation, no adequate data reading was achieved.

In the experiments, sufficient results were obtained for the motor side encoder. However, as the intensity of the vibrations due to the duration of the experiments and the applied torque was increased, some gaps in the encoder readings were encountered. In addition, it was found that the fine tuning of the SEA could not be carried out efficiently to each new unit of the SEA as the number of units increased. This situation was realized after the second SEA that is shown in Fig. 5 is manufactured. Design is modified by replacing the encoder suitable for high vibration in order to account for the vibration problems.

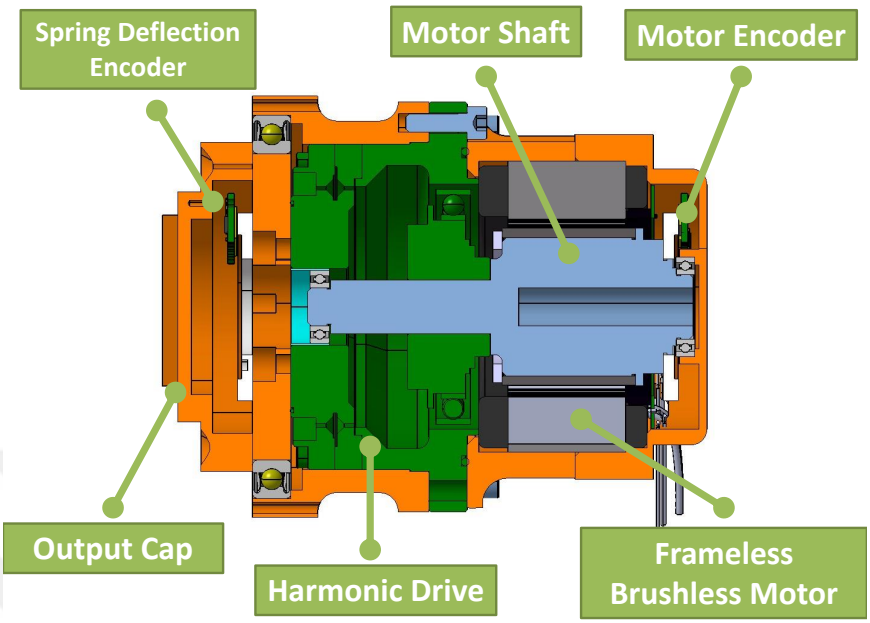

Figure 5: CoEx-SEA version 1.2

A torsional spring is required as the elastic member of the SEA. Therefore, after examining the possible spring types and designs, it was concluded that a torsion based spring can be designed as the elastic member. Several design alternatives were considered in terms of stiffness and load capacity. The design alternatives were evaluated via FEA prior to being tested in the TTM to see the accuracy of the evaluations. Details for the analyses and the experimental procedures will be given in the following sections.

In the first stage experiments, it was found that there was an average of 50% error between the experimental and theoretical stiffness values of the springs. These experiments were carried out at low loads and no transition to the plastic region was observed. The breaking test was started with the known example of the springs that have the lowest stiffness. In the test, contrary to what was expected, the material properties such as the creep resistance point and the transition from the elastic to the plastic region were not observed and there was no noticeable deterioration in

the spring. However, it was observed that the fastener screws were broken due to stretching. In light of these experiments, it was understood that the torsion graph was not linear, and the screws used to connect the spring and the harmonic gear in the system were stretched together with the spring. Due to the size of this extension, the expected linear torque-torsion was not observed from the experiments. Based on the results of the experiment, further studies on the springs structure and improvements to be made on the SEA unit are planned for the next version of the SEA module.

2.3 Spring Design

2.3.1 Topology Selection

Being one of the main elements of the actuator unit, the torsional spring requires a formal design process, in which the stiffness should be linear and durable while containing the weight. Therefore the spring is designed by means of an optimization problem with an objective function that minimizes the spring weight and considering the stiffness as a constraint.

Rotational springs can be listed as twist base [58], bending base [71], and mechanism [72]. As mentioned in [73], bending based springs are more advantageous compared to the torsion based springs such as torsional bars. A bending based spring structure is adopted due its favourable characteristic over twist based structures, e.g. flexibility in defining geometric boundaries [73]. Additional to the stiffness considerations, geometrical boundaries also affect the overall structure of the spring, again in this scenario bending base springs allow flexibility for the actuator. A hierarchical decision on the spring design is necessary to design the spring. At this point, a hierarchical decision must be taken before the spring design is initiated. This relation is simply to define which main member of the SEA is more crucial than the other. In this study, I put the reduction equipment and the actuation unit to the first priority.

Finalization of the spring structure (shape, radius etc.) is directly affected by the decisions on these equipments. In our study the size of gearbox-motor couple is chosen as the geometric boundary limits for the spring topology.

The stiffness value of a spring is affected by the connection elements, such as bolts, flanges, insulators and they also increase the spring related weight. With this in mind, a minimum number of connection elements were targeted in our topology and the spring in Fig. 6(a) is initially obtained.

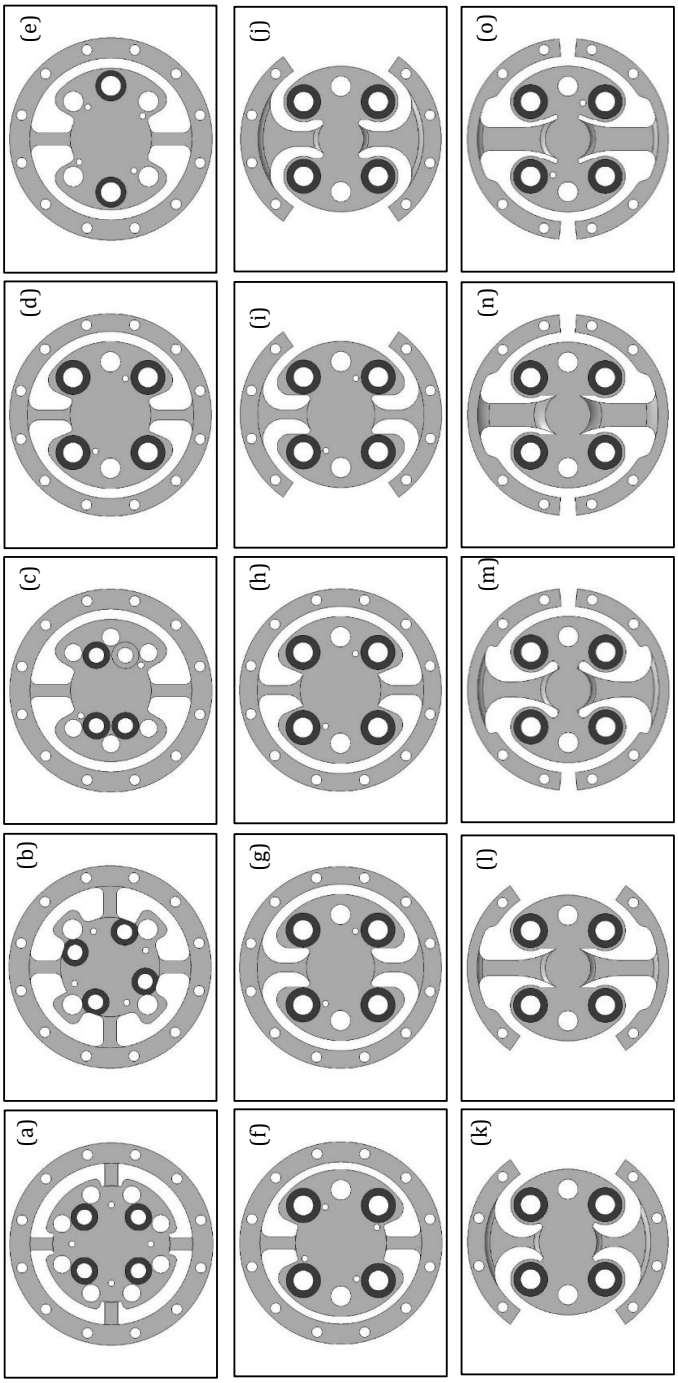

Figure 6: Evolution of the spring topology in a chronological order. Earlier topologies from (a) to (n) do not meet the requirements. From (a) to (f), efficient connection strategy is prioritized. From (j) to (m), the most suitable outer ring was sought. Finally the proposed topology is obtained; see (o)

In order to address the aforementioned challenges, a finite element model of the spring is created. In this model, the torsional spring was modelled using four-noded tetrahedral elements (C3D4) with a shell layer in the outer region of the spring, so as to capture the shear stress in an effective way. C3D4 is a three dimensional (3D) 2-noded element, which has only translational DOFs. There are 5480 shell elements and 14859 solid elements in the model. The bolt holes located at the inner circle were fully constrained (6-DOF), and then 180 Nm torque was applied at the center of the spring, using a one dimensional rigid element and multi point constraint. The purpose of using 180 Nm torque is to assess the elastic and plastic response of the system under the torque load. To fulfil the lightweight design requirement, aluminium is chosen as the material. 6000 series aluminium alloy (Al-6061) is chosen as the grade for its desired fatigue characteristic. In the analysis Poisons ratio of the material is taken as 0.33, while its Youngs modulus and density are 70 Gpa and 270 kg/m^3, respectively.

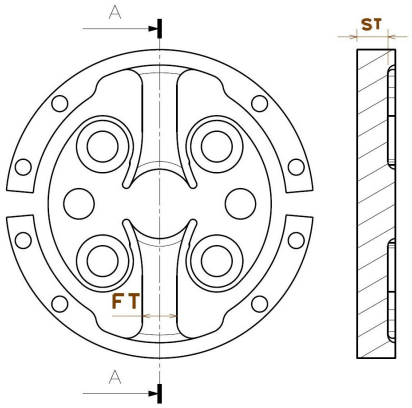

Figure 7: Design parameters (ST and FT) on the finalized spring topology.

The finite element solution was performed in MSC Nastran software using the static analysis tool (SOL 101). Torsional stiffness was calculated as ratio of the torque input to the resulting angle of twist (torsional deflection) as follows,

$$k_{FEM} = \frac{\tau}{\varphi}, \tag{1}$$

where k_{FEM} is the torsional stiffness of the spring, T is the torque applied to the spring and φ is the angle of twist. In addition to the torsional stiffness, the yielding torque is also calculated. For that purpose, the first derivative of the stress-strain curve is calculated and the point on the curve with negative slope is considered as the yielding point [74].

Through the iterations from Fig. 6(b) to Fig. 6(f), possible connection variations are tried to minimize the connection member without affecting the stiffness. In the final design, the center screws are replaced by custom made pins to minimize the necessary surface area.

In defining the spring stiffness, I aimed for a maximum $\approx 2^\circ$ of deflection under the maximum torque load of $164Nm$ based on our prior experiments [19]. The softer springs may provide better torque measurement quality; however, their influence in robot dynamics become more dominant and they limit position control bandwidth. To this end the spring evolution provided in Fig. 6 also included an empirical search for the optimal feder shape, such that they are long enough to provide quality (high fidelity) deflection reading without transiting to the plastic region. In addition, the number of the feders were reduced to two for the sake of increased elastic deflection without generative extensive moments. Finally the spring design in Fig. 6 (o) met all the conditions, namely, longer feders, reduced center ring size, easy-to-manufacture. As an example, the torsional deflection under $112Nm$ torque loading is shown in Fig. 8 ($FT = 9mm, ST = 8mm$). The resulting torsional stiffness for this design is $91Nm/deg$.

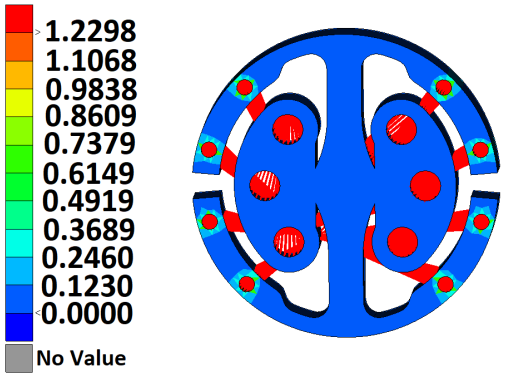

Figure 8: Deflection results for 112 Nm input torque, from FEA

2.3.2 Experimental Verification of Spring Design

In order to experimentally verify the spring properties, I have used a TTM; see Fig. 9). During the experiments, a mock-up version of the springs connections from harmonic drive (HD) to output shaft was adapted to the TTM. The stiffness values of these mock-up elements were sufficiently high to avoid coupling effects.

Experiments were performed in two steps. In step 1, the stiffness of the spring was tested via TTM to verify the simulation study presented in Section 2.3.1. In step 3, a torsional break-up test was performed in order to characterize the plastic behaviour of the spring.

2.3.2.1 Stiffness Test

In this experiment, the spring was tested under the same torque values that were used in the simulations. Torque inputs were set to ensure that specimen yield strength was not exceeded. The comparison between the experimental and simulation results is depicted in Fig. 11. The results indicate an highly satisfactory correlation up to the torque level of $112Nm$. Moreover, it were observed that the spring stayed in the elastic region up to $1.8°degrees$, which was one of the major design objectives. Consequently, no permanent deformation nor fatigue was observed, as the spring did not switch to plastic region. The stiffness target of $91Nm/deg$ was also met.

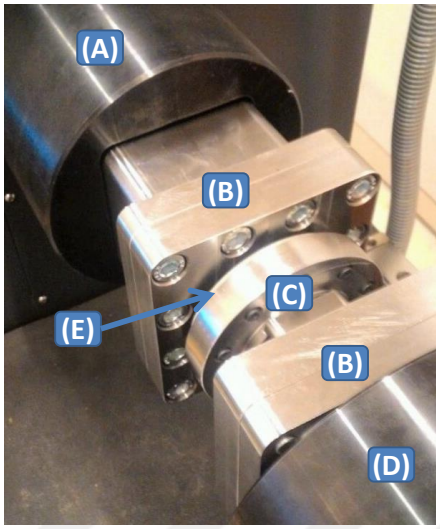

Figure 9: Experimental Set-up: (A) TTM's variable speed drive loading system head, (B) Stiff connectors, (C) mock-actuator cap, (D) TTM's strain gage torque sensor mounted weighing head (E) Spring specimen

As a result of this test, I observed that our design approach provides a spring that can act as a reliable torque sensing element as its stiffness stays constant for a large portion of the elastic region. Though I set the stiffness of the spring to a specific value, different stiffness requirements can be met by altering the ST and FT parameters. For that purpose, an empirical equation that utilizes and ST, FT parameters can be derived for the entire elastic region.

2.3.2.2 Break-Up Test

In this experiment, torque input was gradually increased until the spring and/or its connections failed. This was done intentionally to observe the instant when the spring transitions to plastic region. Fig. 12 displays the plastic deformation pattern of the spring.

As may be seen in Fig. 11, the transition from elastic to plastic characteristics occurs corresponding to the angular deflection of $1.8°degrees$. After this angular deflection value, the first break-up was observed when the applied torque was 240 Nm;

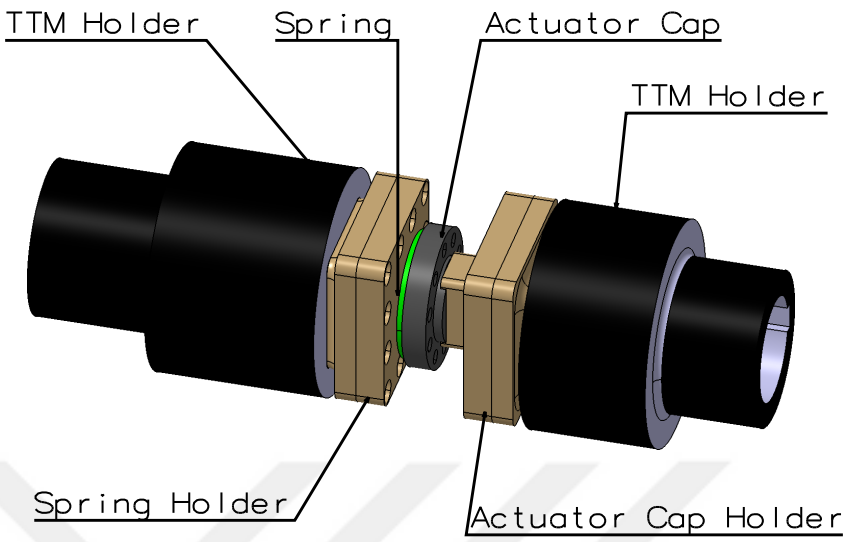

Figure 10: TTM CAD drawing

see Fig. 11. Since this amplitude is considerably more than the torque output capability of CoEx-SEA, the designed spring is deemed to be suitable for our applications; see Fig. 12 (A) and (B) for the broken specimen after the break-up experiment.

2.3.2.3 Strain Rate Test

The frequency of the torque applied range may differ [19, 75–77] in accordance with the application area. Our initial simulation and experimental studies indicate that the torque control bandwidth can be as high as 25 Hz [78]. As previously mentioned, the main deflection characteristics depend on the feder bending, therefore, the modulus elasticity of the material plays a dominant role. In this view, stress-strain relation can be used for the differentiable loading effect as below [74]:

$$\sigma = C\dot{\epsilon}^m \tag{2}$$

Due to limited loading rate at the TTM, I used the method explained in [74] to analyse the higher frequency effects of differentiable loading. Two aluminium 5000

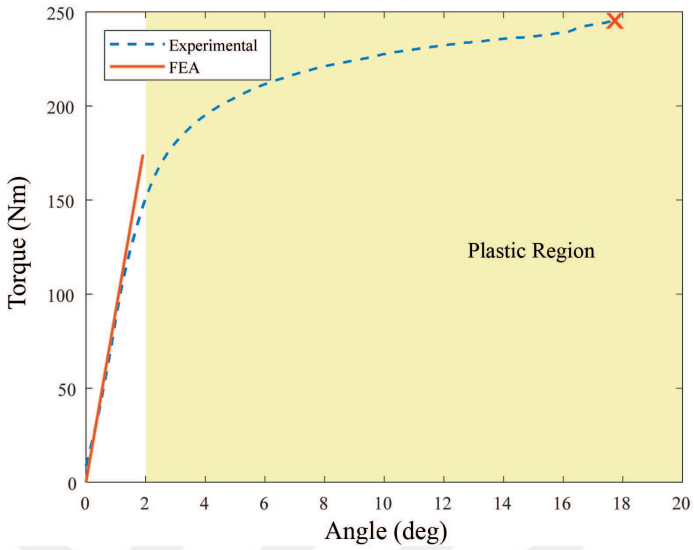

Figure 11: Stiffness test via TTM: Comparing the experiment and simulation results.

series specimen with $FT = 8.8mm$ $ST = 8.0mm$ were tested in TTM under the two limiting loading rates as $1mm/deg$ and $5mm/deg$. The strain rate is given in the following,

$$m = \frac{ln(\sigma_2/\sigma_1)}{ln(\dot{\epsilon}_2/\dot{\epsilon}_1))}, \tag{3}$$

where m is the strain rate σ is stress and and the $\dot{\epsilon}$ is the strain rate. The subscripts 1 stands for the stress and strain rates for loading rate of $1mm/deg$ while the subscript 2 stands for the loading rate of $5mm/deg$.

$$\sigma = \frac{Mc}{I} = \frac{\tau c}{I} \tag{4}$$

where c and I are respectively, the distance between neutral axis and the centroidal axis, and the M is the bending moment. However, since the feder's end tip is located in the outer torque line, output torque τ is equal to the M. Thus the relation between the torque and the normal stress is defined as follows,

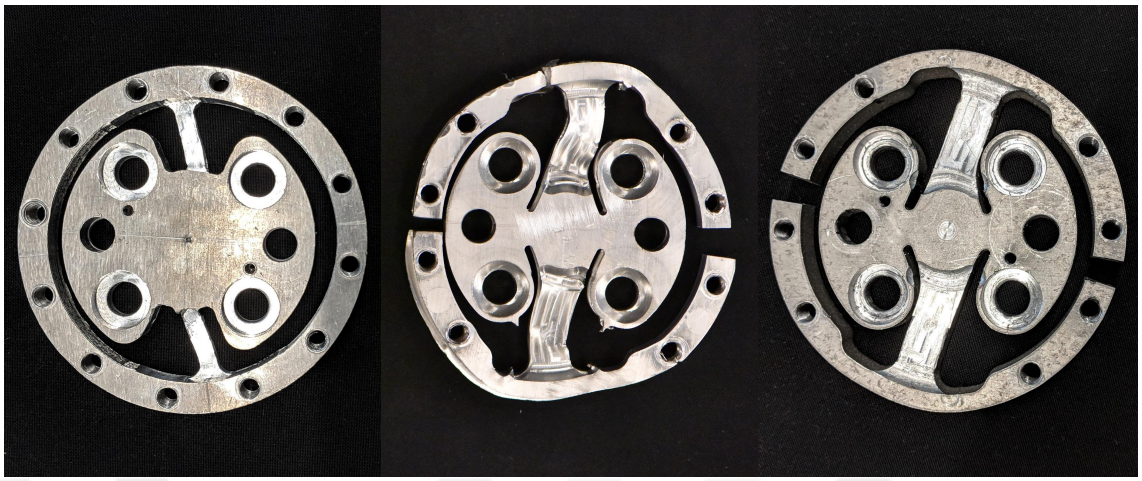

Figure 12: (A) Spring topology-h after stiffness test (B) Spring topology-o after break-up test (C) Spring topology-o after stiffness test

$$\epsilon = \frac{\theta c}{L}, \tag{5}$$

Eq. (5) represents the relation between strain and the twist angle θ. By taking the c and feder length L value constant we yield the following,

$$\dot{\epsilon} = \dot{\theta} \tag{6}$$

Strain rate can be interpreted as the twist angle rate. By placing the (4) and (6), into (3), m value can be defined as below;

$$m = \frac{ln(\tau_2/\tau_1)}{ln(\dot{\theta}_2/\dot{\theta}_1))} \tag{7}$$

In Fig. 13, five random points are selected in the plastic region. By comparing the twist angle rates and torque values of these randomly chosen results, five distinct m values (m1-m5) are calculated in accordance with (7). Even though a single m value is also sufficient to reduce the possible numerical errors, an average of m values are taken into account. Afterwards, this deduced value is used in a reverse manner in

(7) to predict the response of the same topology for a higher loading rate. Predicted response of the specimen can be also seen in Fig. 13 for the loading rates of $0.5Hz$, $1Hz$, $10Hz$, and $25Hz$.

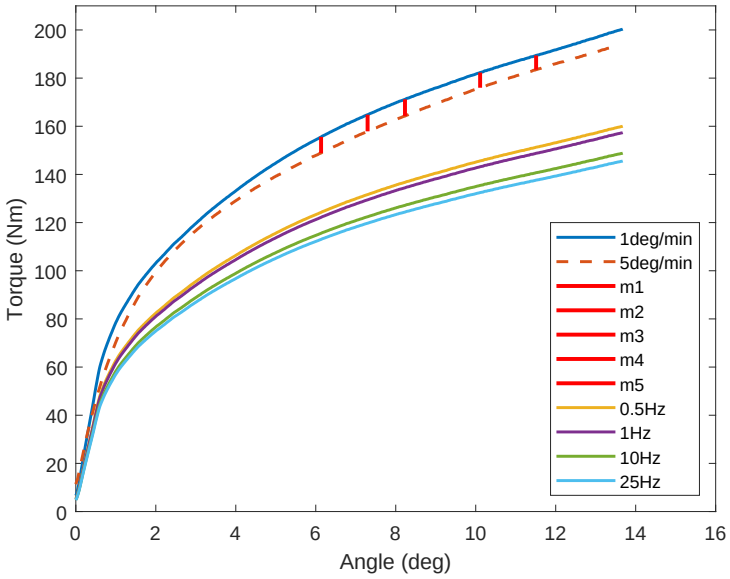

Figure 13: Experimental results on twist rate at different loading speeds and forecasted torque-torsion relations for higher rates

With the result of this analysis, one can obtain the corresponding stiffness curve in accordance with the given application domain.

2.3.3 Stiffness Parametrization

In order to formulate the torsional stiffness of the spring with respect to ST and FT, a regression was performed using the final spring topology displayed in Fig. 7. I defined 52 distinct spring models by changing the FT and ST parameters. Torsional stiffness of the aforementioned spring models were calculated using the finite element model described in Section 2.3.1. Afterwards, the torsional stiffness values corresponding to 52 springs, with various ST and FT parameters, are used to derive an empirical equation relating torsional stiffness and the maximum allowable torque.

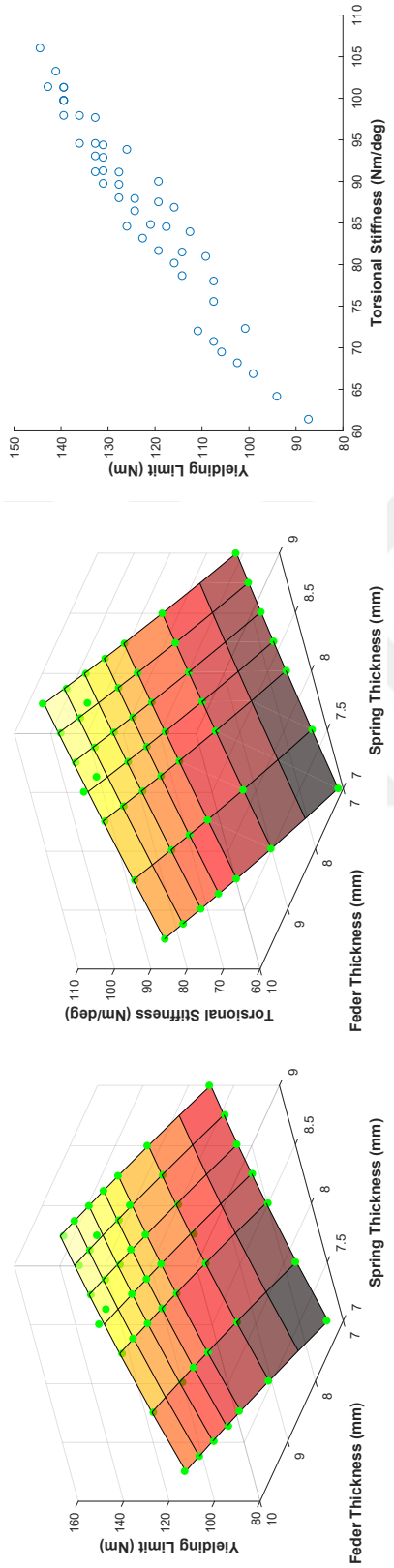

Figure 14: The empirical model of (A) yield limit (B) torsional stiffness (C) stiffness yield limit relation

A quadratic empirical equation is derived chosen as, given in (8) and (9) due to its higher correlation than the quadratic form. Empirical models are shown in Fig. 14.

$$\begin{aligned} k_{EMP} &= -8.5 - 0.34ST^2 + 0.52FT^2 + 3.42ST \\ &- 4.34FT + 1.03STFT \end{aligned} \tag{8}$$

$$\begin{aligned} \tau_{EMP} &= -184.15 - 1.45ST^2 - 0.63FT^2 + 29.99ST \\ &+ 18.27FT + 0.71STFT \end{aligned} \tag{9}$$

The quality of the empirical equation was firstly tested on four cases with different FT and ST parameters, which were not used in the determination of the empirical equation; see Table 2. The torsional stiffness from the empirical equation is compared to those calculated from the finite element model. The results show that quadratic empirical equation can predict the torsional stiffness of the spring quite accurately. The relative error (δ) between the quadratic empirical equation and the finite element model range from 0.1% to 1.5% in four cases.

ST (mm)	FT (mm)	k_{FEM} (Nm/deg)	k_{EMP} (Nm/deg)	δ (%)
7.25	7.25	65.5	64.5	1.5
8.25	7.25	71.1	71.2	0.2
8.25	8.65	88.4	88.5	0.1
9.00	8.65	93.3	93.4	0.1

Table 2: Relative error between empirical equation and FEA for four distinct spring models

A torsional deflection of 1.8° is targeted under the application of the maximum torque of 164 N.m. This corresponds to a torsional stiffness target of 91 Nm/deg. This torsional stiffness target can be achieved by using design parameters $ST = 8$ mm and $FT = 9$ mm, using (8).

2.3.4 Fatigue

Having determined stiffness characteristics and elastic/plastic region boundaries, I assessed the fatigue life of the spring, see Fig. 15. To this end, rather than considering constant valued torques, e.g. see [79], I make use of the experimental data provided in [19], since our application domain is exoskeleton robots.

Finite element model of the SEA including the boundary conditions described in Section 2.3.3 is analyzed under 1 Nm applied torque. Fatigue strength of the Al-6061 is 96.5 MPa under $5 \cdot 10^8$ completely reversed stress cycles [80]. The maximum principle stress is used in the fatigue life prediction of our model.

The Palmgreen-Miner cumulative fatigue damage theory, also known as Miners Rule, is used to determine the fatigue life for SEA module as follows [81], under the operational loading data provided in [19]. In accordance with the Miners Rule, accumulated damage is calculated as follows

$$C = \frac{n_1}{N_1} + \frac{n_2}{N_2} + \cdots + \frac{n_i}{N_i}, \tag{10}$$

where n_i is the number of cycles at the i^{th} stress level, N_i is the number of cycles to failure corresponding to the i^{th} stress level. n_i/N_i is known as the damage ratio at the i^{th} stress level. The parameter C is taken as unity corresponding to failure [81].

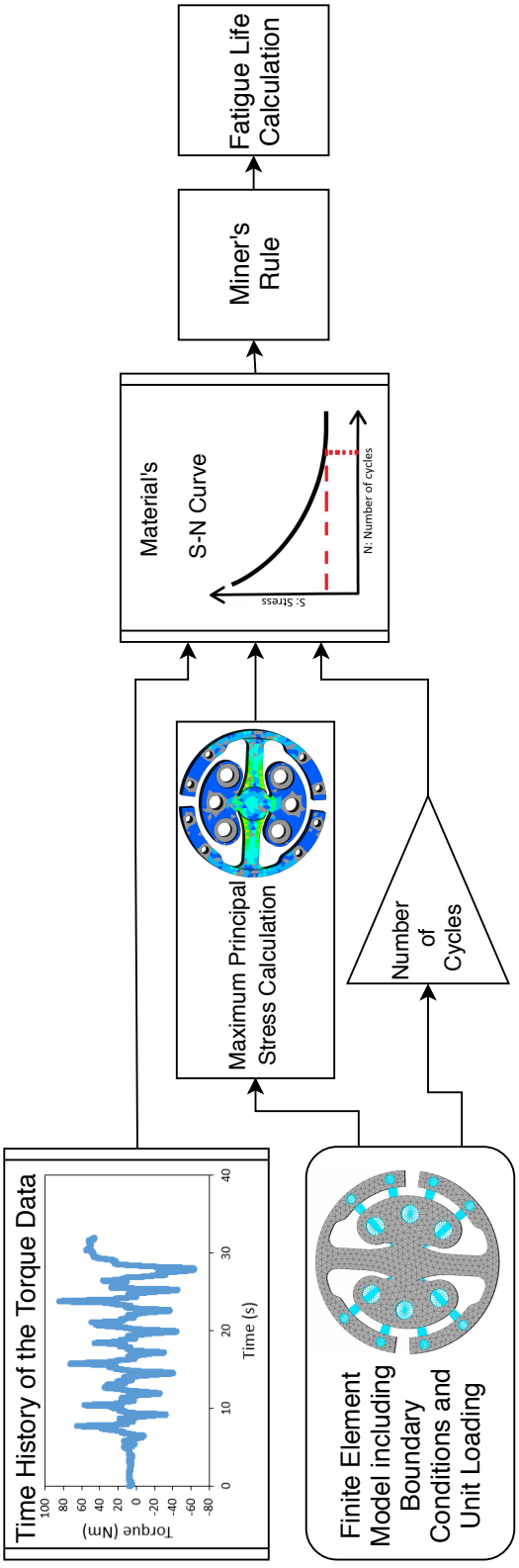

Figure 15: Fatigue life calculation method

The damage values corresponding to the loading are depicted in Fig. 15. The maximum fatigue damage occurs on the inner radius of the part with a damage value of $4.35 \cdot 10^{-6}$. Therefore, the loading could be applied for $1/(4.35 \cdot 10^{-6}) = 2.297 \cdot 10^{5}$ cycles. Since the period of a sample cycle torque data is $32sec$, the spring can be operated for 1914 hours continuously (79 days), under the loading provided in [19].

The geometry of the SEA spring is iteratively modified to reduce the stress concentration factors. The maximum von-Mises stress corresponding to the final design is 172 MPa. Material of the spring was also changed to the Al-7075 which have 159 MPa fatigue strength. The distribution of the damage profile corresponding to the loading is shown in Fig. 11. The maximum fatigue damage occurs on the inner radius of the part with a damage value of $2.2 \cdot 10^{-7}$. Therefore, the loading could be applied for $1/(2.2 \cdot 10^{-7}) = 4.55 \cdot 10^{6}$ cycles. Since one cycle of the torque data is 32 seconds, this corresponds to about 97916 hours of operation (1579 days) for the mentioned loading.

2.4 Thermal Analysis

In implementing high power SEAs to robots that physically interact with humans in a continuous manner, e.g., exoskeletons, dissipating the generated heat is of importance. The performance of the actuator varies with respect to the temperature of the surrounding space and heat generated by the actuator unit itself. In particular, the magnetic flux density is affected by the temperature and may degrade the system performance. Further limitations of insufficient thermal management may cause undesired effects on the electronic components and actuator parameters that cause uncertainty in modelling. To this end, many researchers proposed active cooling systems [43, 62–64, 82]. The literature also shows that actuation units used in robotics can reach high temperatures in short process time [82], which affects the performance quality.

2.4.1 Thermal Simulation

CoEx-SEA unit was firstly simulated on ANSYS Icepak electronic cooling software in order to obtain the thermal map of the system. This approach is considered to be effective in the case where further improvement is needed due to thermal performance. In the thermal model, the stator was represented as a power source for the heat generation as it includes the windings; see Kollmorgen TBMS frameless brushless motor series [1]. The heat flows from stator to the frame and to the rotor. Furthermore, a total of 2352000 Hexadron type elements were used in the model. A constant temperature of 34°C was given as the input source and a steady state simulation is performed. This simulation shows the transfer path of the generated heat and the passive cooling capacity of the SEA.

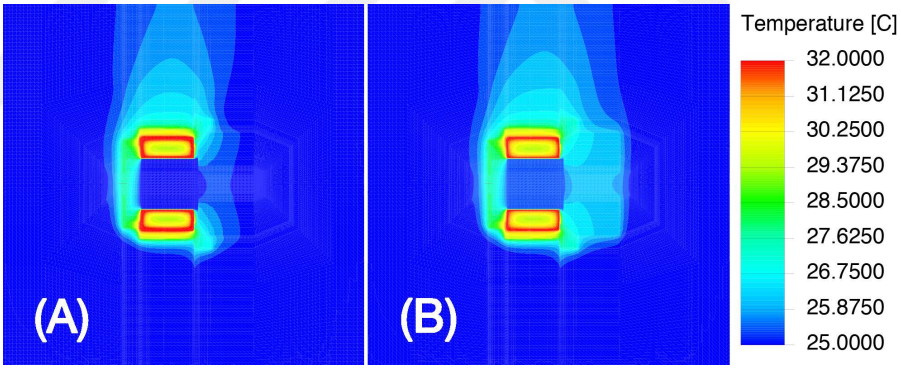

Figure 16: Temperature flow of the actuator: (A) simulation at t = 38.25 s (B) simulation at t = 497.3 s

For the second simulation study, a steady state analysis was performed under 105°C temperature, which is the maximum temperature the actuator is designed to operate. The residual error tolerance for the simulation was set to 10^{-6}. Temperature at three different locations of the actuator model was monitored throughout the simulation. Point 1: the location where most of the embedded electronics reside,

[1] https://www.kollmorgen.com/en-us/products/motors/direct-drive/tbm-series/

point 2: the outer surface of the actuator, which acts as the thinnest insulator between the motor and its surroundings, point 3: the output spring of the actuator. Fig. 17 displays the temperature distribution at these locations as a function of time. The results of this simulation showed that the system is not able to cool SEA passively under constant maximum heat generation. In order to investigate the root-cause, a transient dynamic analysis was performed. To that end, an exoskeleton-supported human walking experiment data was employed [19]. As the heat source input, the exoskeleton's hip joint torque variation was taken into consideration. The simulation was run until the system reached to a steady state solution. Fig. 16(A) shows the starting state and Fig. 16(B) shows heat distribution of the SEA when the point 2 is reached the steady state. The results of this dynamic thermal simulation prove that the actuator is capable of maintaining cooling capacity under actuator's operational conditions.

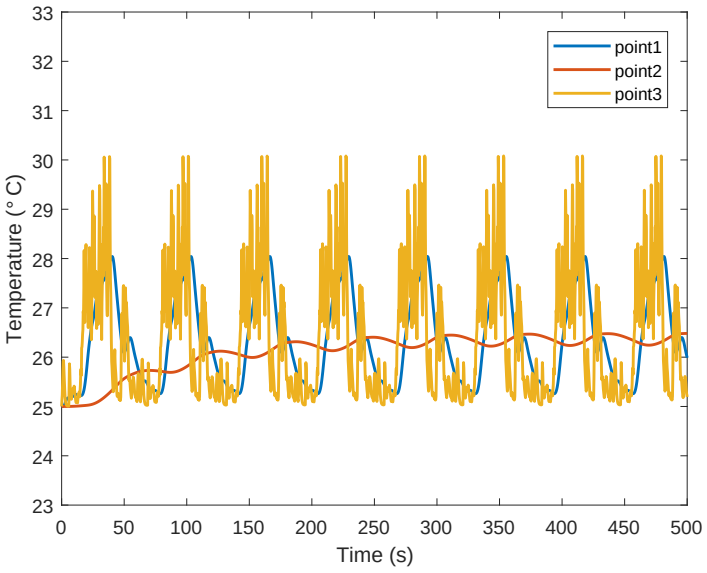

Figure 17: Dynamic thermal analysis results simulation.

2.4.2 Thermal Behaviour Experiments

Thermal behaviour experiments were performed in order to verify the simulation results. However, due to the lack of the hardware specifications provided by the manufacturers, possible improvements for the thermal model of the SEA was limited. Thus, we decided to use the experimental method proposed in [83]. The experimental setup and hardware used in the experiments are shown in Fig. 18

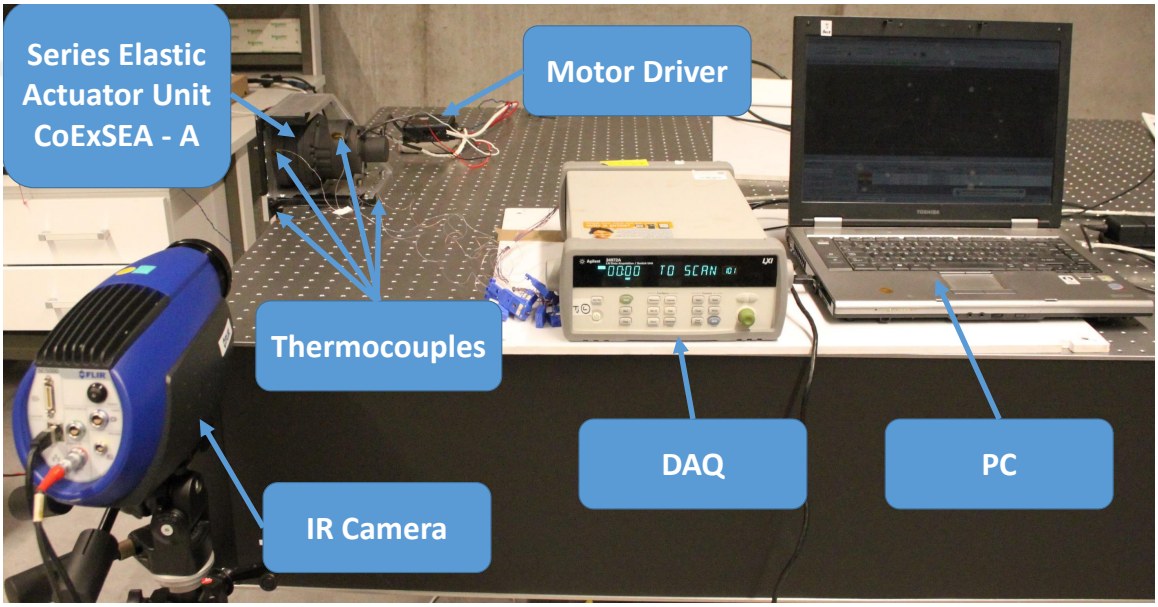

Figure 18: Experimental setup for the thermal experiment.

A Flir SC5000 IR camera with wavelength range of $2.5\mu m - 5.1\mu m$ and sensitivity up to 20 Mk was employed. The measurement system has an accuracy of 1% for temperatures less than $15°C$. In addition, a data acquisition device (Agilent 34972A LXI) with Omega T-type thermocouples are used to verify the data collected from the IR camera. The accuracy of aforementioned thermocouples is $1°C$. Prior to the experiments, SEA module was painted in black with emissivity of 0.98 to pull all different components to the same emissivity level. IR thermography software was calibrated with respect to this emissivity level.

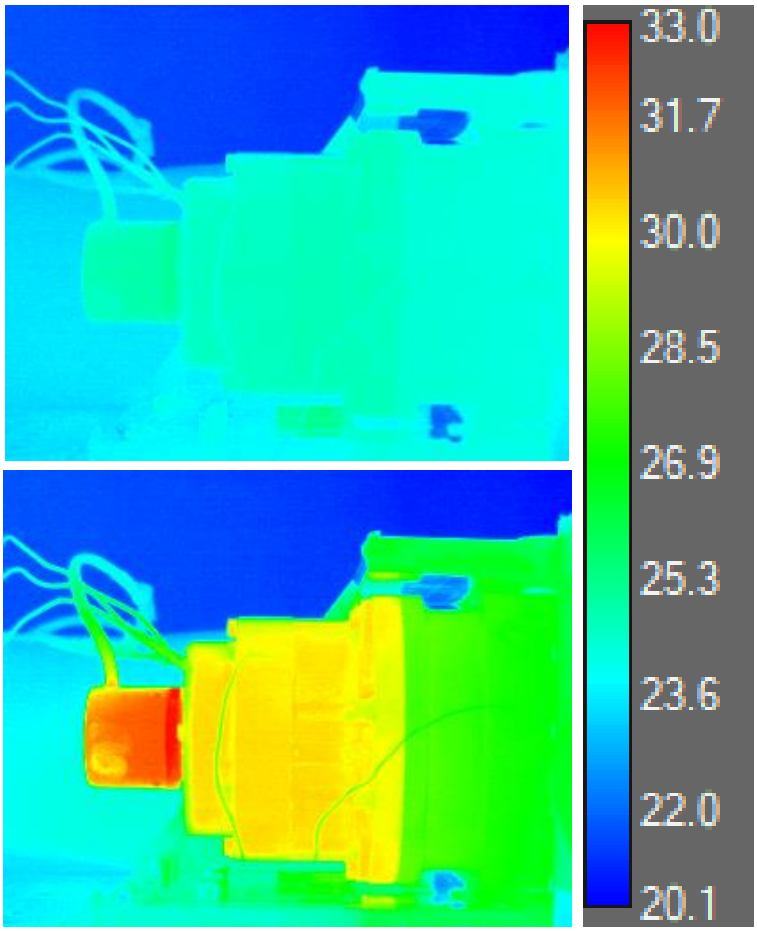

Figure 19: IR image of the SEA module at (A) $t = 30s$, (B) $t = 19min$

The results in Fig. 20 show that the heat transfer between the heat generating members (DC motor, encoder, etc.) and the other components of the SEA module is not significant. This finding is verified by comparing the results from thermocouples and IR thermography and this is plotted in Fig. 21.

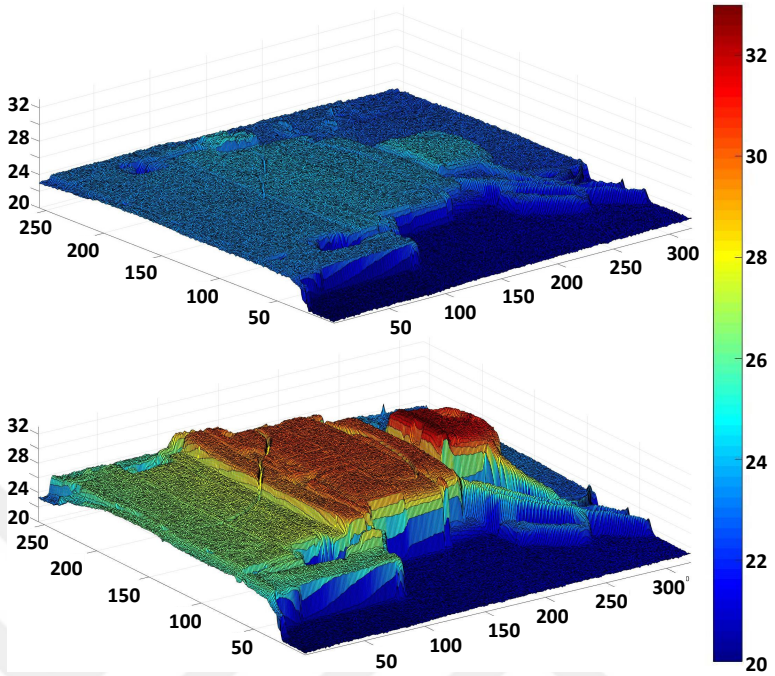

Figure 20: 3D temperature plot of the SEA at (A) $t = 30s$, (B) $t = 19min$

After the tests are repeated for several trials while considering the safety of the experimental setup, for the response of the system for longer time spans modeled with respect to Newton's Law of Cooling/Heating is as follows,

$$T(t) = T_c + (T_o - T_c)e^{-dt} \tag{11}$$

In (11) $T_c = 34.27°C$, $T_o = 23.97°C$, and $d = 0.03988$. This model shows that the temperature of the SEA where it is in close proximity to the human-user will converge to maximum value of $34.27°C$. This value is sufficiently lower than the maximum suggested operation temperature limit for the Kollmorgen TBMS 7631 brushlees DC motor, see Fig. 22 .

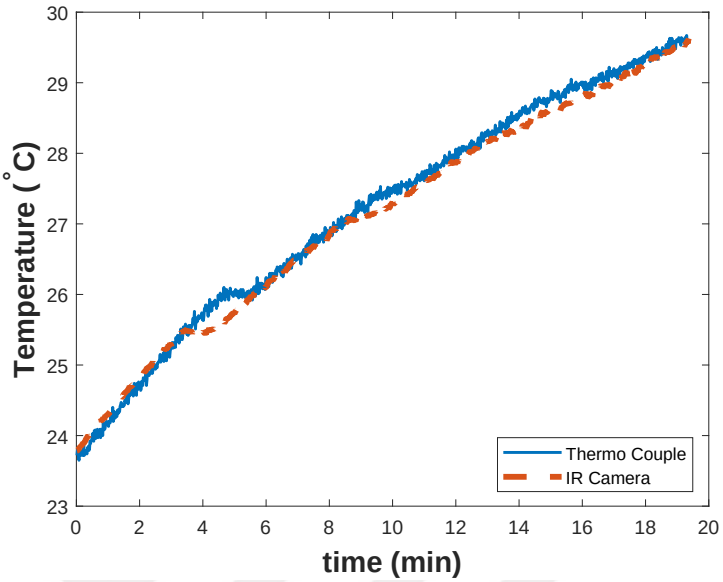

Figure 21: Temperature data of the SEA for 19min, experiments

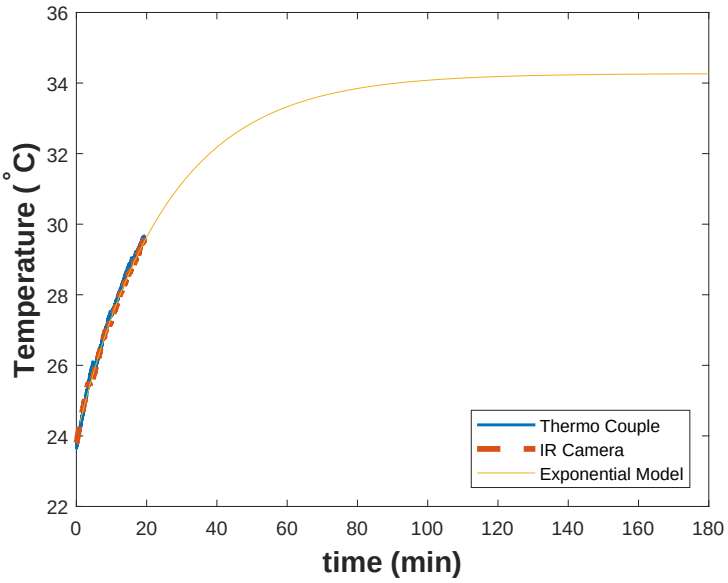

Figure 22: Heat transfer model via Newton's law of cooling

2.5 Torque Control Implementation

Torque control problem of the SEA can be converted into a position control problem due to a linear relationship between the deflection of the spring and the output torque of the actuator [84]. Even though straightforward control methodologies can be used in controlling such actuators, the torque control problem of the SEA is still an active research area due to its complicated dynamics. There are robust control techniques in the literature to improve the torque tracking performance of the SEA, even its subjected to various uncertainties. The cascaded control scheme for the SEA was proposed in [85] and [86] is adopted due its proven high bandwidth control performance.

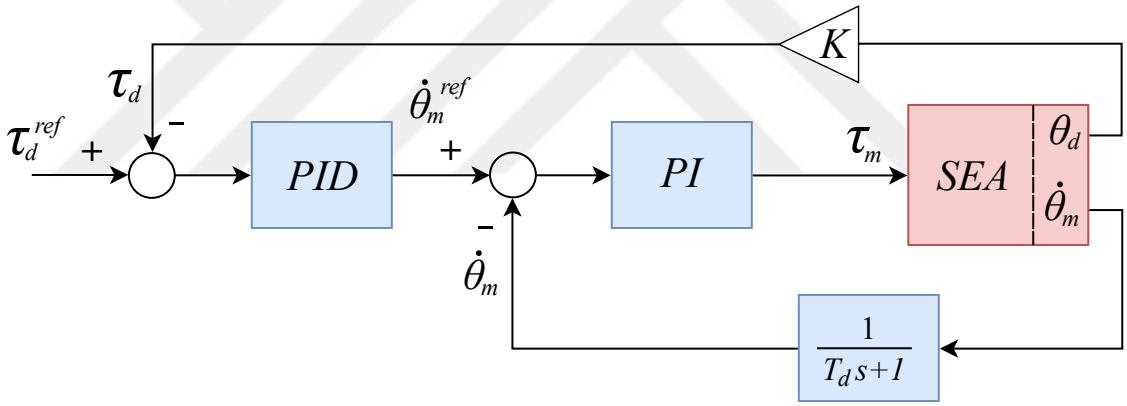

Figure 23: Cascaded control with an inner velocity loop [1]

In the controller scheme, there is a higher speed inner velocity loop and an outer feedback torque control loop. The block diagram of the controller can be seen in Fig. 23 where θ_d is deflection, $\dot{\theta}_m$ is motor velocity, K is the spring constant, τ_d and τ_m are the output torque and the motor torque respectively. The inner velocity loop is controlled by a PI controller while there is a PID controller in the outer loop. Motor velocity is derived from the motor position encoder data and the low pass filter with T_d time constant is implemented to filter the noise. The tuning process of the

controller was achieved with respect to proposed stability boundaries in [1].

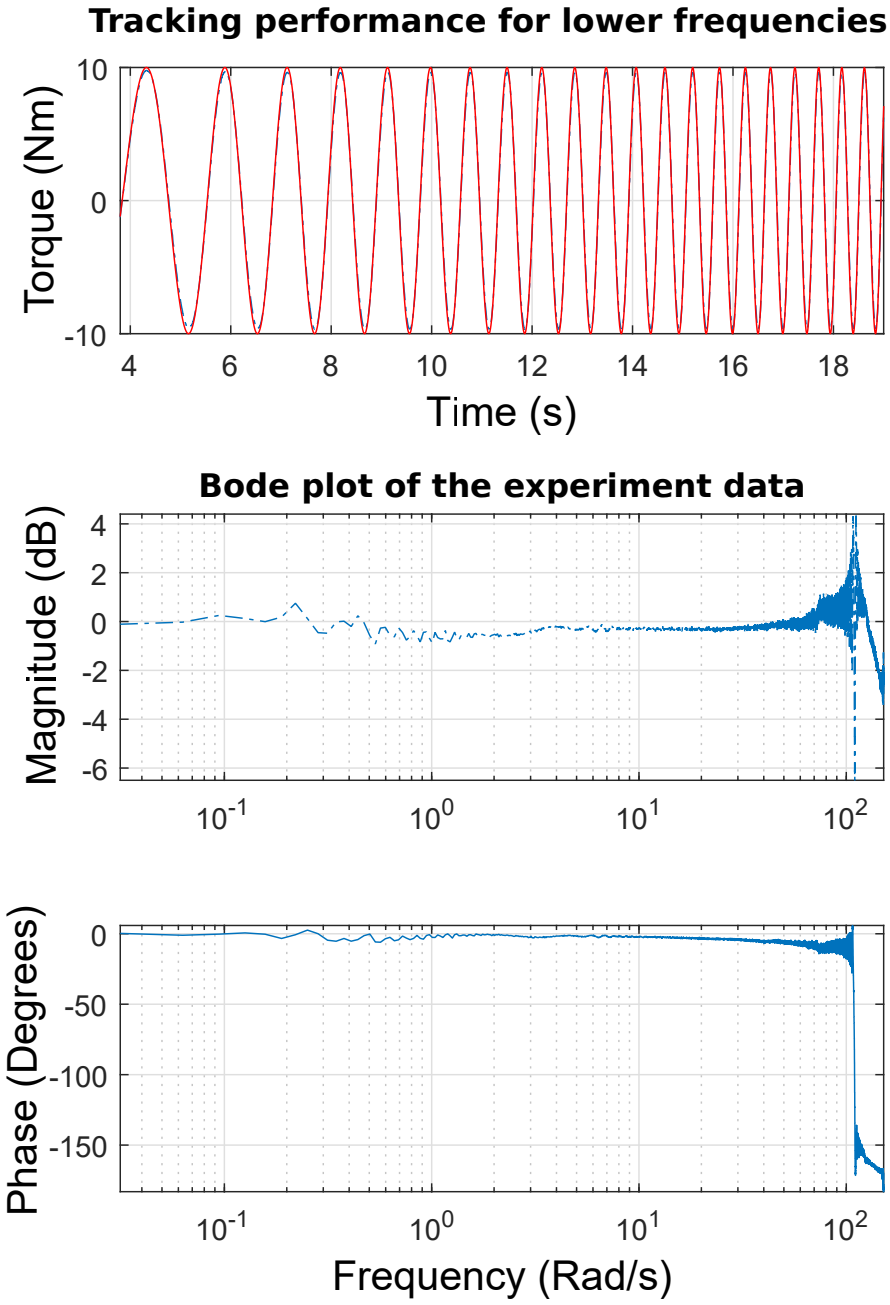

Figure 24: Above, the tracking performance of the chirp torque reference, below the bode diagram of the controller.

The tracking performance for the low frequency chirp signal can be seen in Figure

24. The bode diagram of the controller is constructed to visualize the tracking performance of the controller and can be seen below the tracking performance. Controller is able to provide relatively robust tracking performance with the bandwidth up to 17 Hz. To conclude, it is experimentally observed that the SEA unit achieves fien torque control. In the experiment, the gains of the controller were as follows;

	P	I	D
PI	0.045	0.012	-
PID	16	7	0.08

Table 3: PI and PID controller gains

2.6 Concluding Remarks

After the control experiments and long duration performance data, the following problems were diagnosed:

- Single unit design is hard to assemble and dissamble. When an inspection or maintenance needed, this block design causes problems.
- Unpredicted lateral forces may affect the spring structure thus the spring stiffness.
- For the unit CoEx-SEA-B mass-to-torque ratio cannot be improved with the previously selected gearbox.
- Increase in the length of the rotor shaft increases the possible assembly problems.

By evaluating these main points, these listed final improvements were done on the design:

- Motor side re-designed as a single unit
- Rotor shaft is made shorter.

- HD unit is changed with a newer and a lighter version
- Spring is supported with an additional bearing

CHAPTER III

SPRING-SUPPORTED ANKLE JOINT

A possible solution to the problems caused by the underactuation is to make use of spring-supported passive joints [87, 88]. Since the robot-aided paraplegia walking support includes predetermined trajectories, one may exploit the passivity property via offline simulations to come up with an optimum stiffness value that provides relatively more efficient locomotion. An exemplary work that exploits the spring potential was provided by Tsagarakis et al. [55], where the stiffness values were optimized for maximum energy efficiency of a humanoid with SEA . A similar approach was executed by exploiting the base resonance frequency to generate hopping locomotion [89]. Springs were also coupled with clutch mechanisms to provide power assistance [90].

Despite the prove efficacy of passivity in the legged locomotion research, only a handful of exoskeleton systems are equipped with springs [88]. Considering the fact that the recent trend in exoskeleton hardware development suggests increasing the number of active joint for greater motion flexibility, I argue that spring-supported passive joints may provide the same effect while reducing the power consumption, weight and size. The stiffness tuning on the other hand has not been fully addressed and this chapter aims to contribute towards this direction. In addition, user-specific stiffness tuning metrics were not investigated, to the my knowledge.

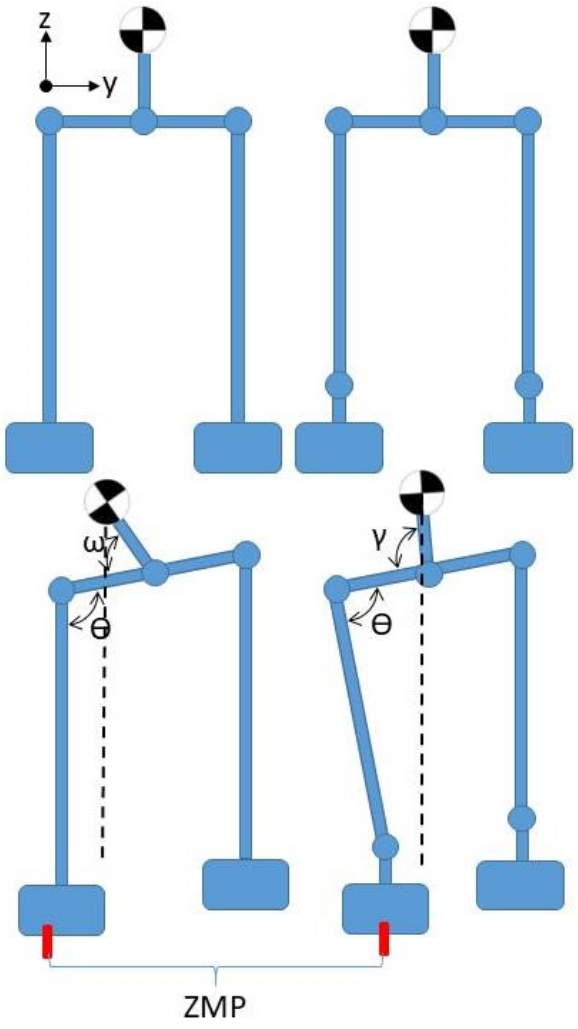

Figure 25: The changes in ZMP and upper body torso angle with the addition of an AI/E compared to a fixed ankle joint. For the case of no passive AI/E joint, the HA/A rotation must be large to provide the desired CoM position. In contrast, for the case with passive AI/E joint, the HA/A joint rotates less as the AI/E joints also contributes. As a result, both torso angle and ZMP can be well contained.

In [38, 39], it is shown that the the minimum requirement to realize 3-D walking motion is by equipping each leg with 4 active joints, namely, a 2-DOF hip joint along the F/E and A/A axes, a 1-DOF knee joint along the F/E axis and a 1-DOF ankle joint along the F/E axis. While this joint configuration provides the means for a kinematically feasible walking motion, the upper body orientation along the lateral

axis is relatively large when compared to a healthy person's upper body motion; see Fig. 25. This leads to aggressive changes in the ZMP, an important balance criterion to assess the consistency of walking motion [91].

In the light of the facts discussed above, this chapter presents a framework to optimally tune the stiffness values of spring-supported passive joints of exoskeletons. In particular, I focused on the 4-DOF-per-leg model provided in [38, 39], and added a spring-supported passive ankle joint along the Inversion and Eversion (I/E) axis. Using MSC.ADAMS and MATLAB co-simulation, an optimization routine was devised to explore the optimal stiffness value that minimizes ZMP to improve active balancing. For a given target sway trajectory, I showed the variance in optimal passive joint stiffness values with respect to overall mass and height of the combined human-exoskeleton system in question.

3.1 Stiffness Analysis

3.1.1 Method

3.1.1.1 Compliant Body Modeling

An MSC.ADAMS (version 2016) model was developed to simulate dynamics of the system, where the equivalent parameters representing the combined human and exoskeleton system such as mass, inertia were used; see Fig. 27. The input data for exoskeleton parameters were obtained from the modular design of Bartenbach et al. [87], in which CAD data for an exoskeleton with 8 active joints was shared publicly. The actuator specifications were obtained from [75], whereas, human parameters were obtained from [92] and [93]. The following modelling approach was taken into account to model distance between Hip A/A and Hip E/F joints: The femur head was accepted as the HA/A joint's rotation axis and the Hip Flexion And Extension (HF/E) joint to HA/A joint length value was adjusted in accordance with the distance between fovea capitis and greater trochater of the femur; see Fig. 26. Additionally, in

accordance with the data presented in [94], maximum deflection of the ankle's passive joint was limited to 20°.

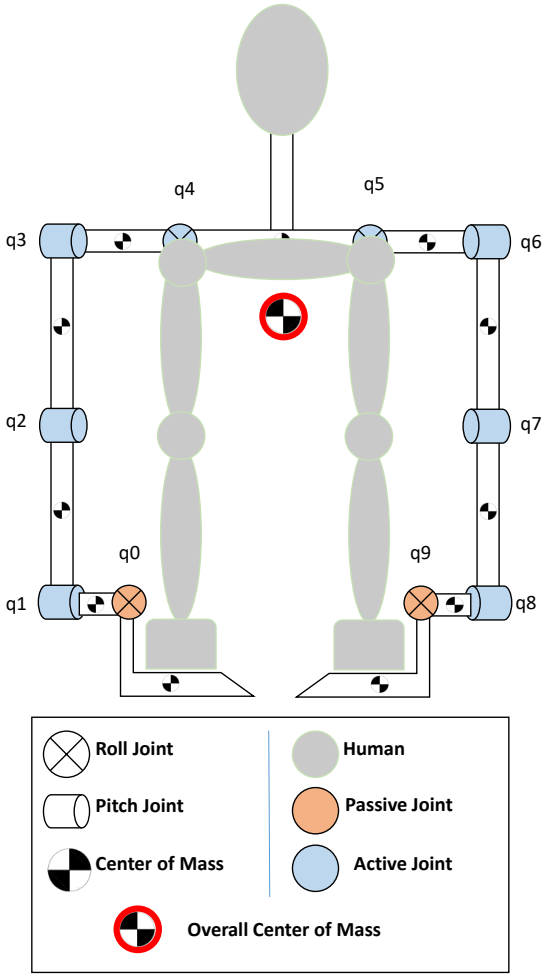

Figure 26: Modeled exoskeleton links and human limbs with their respected CoM positions, red point represents the combined BCM of the joint human-exoskeleton model

As depicted in Fig. 28, reaction torques from the passive joints of the system were calculated in MATLAB. MSC.ADAMS model was exported as a plant model to MATLAB/Simulink using ADAMS.Controls plug-in, where the inputs to the model were active joint angles and the torque values created by the passive springs on the AI/E joints. The outputs were the angular displacements and the angular velocities of the AI/E joints and the Reaction Force (Fz) and Pitch Moment (Mx). For every

time step, the torques were calculated from Simulink and sent to MSC.ADAMS. Similarly, MSC.ADAMS model calculated the angles of the joints and sent the results to Simulink. MSC.ADAMS macro codes were developed in order to facilitate the development and adjustment to humans of different sizes. In all cases, the mass of the exoskeleton was considered as the same. The MSC.ADAMS model was developed as capable to calculate the equivalent mass and inertia for the combined human-exoskeleton system for different subjects based on given total body weight and the body height with respect to average human body ratios given in [92] and [93]. CAD drawings of the components were not associated with the rigid bodies in the model in order to reduce the computational complexity of the simulation.

As previously mentioned, inertia and mass properties were calculated separately, then were considered as the inputs to the MSC.ADAMS model. Rigid body models were represented with their mass and mass moment of inertiae located at their respective CoM. Mass moment of inertia values were defined with respect to the body moving coordinate system at the CoM. The MSC.ADAMS model of the system is shown in Fig. 27. The model has 25 members, 10 revolute joints, 14 fixed joints and 8 general motion constraints to prescribe the kinematics of the joints resulting in a 8-DOF system. The overall mass of the model is 138 kg (100 kg human and 38 kg exoskeleton) and CoM of the model is shown in Fig. 26, MSC.ADAMS-MATLAB/Simulink co-simulation environment is shown in Fig. 28.

Table 4: Structure and the stiffness parameters of the analysis model

		Structure	Torque Capacity	Stiffness
1	AI/E	Passive	—	TBD
2	Ankle Flexion and Dorsiflexion (AF/D)	Active	95 (Nm)	5220 (Nm/rad)
3	Knee Flexion And Extension (KF/E)	Active	95 (Nm)	5220 (Nm/rad)
4	HF/E	Active	95 (Nm)	5220 (Nm/rad)
5	HA/A	Active	95 (Nm)	5220 (Nm/rad)

The impact function of MSC.ADAMS was used in order to model the interaction

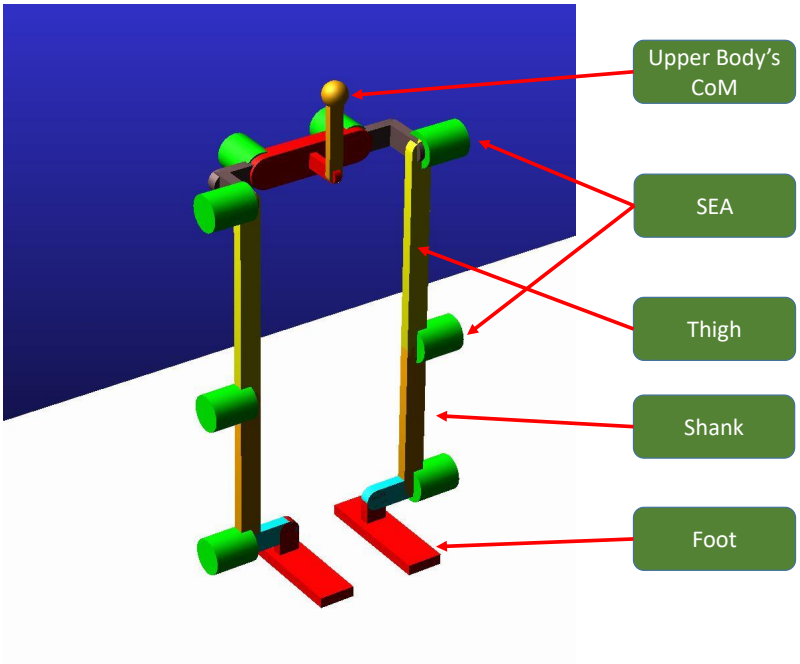

Figure 27: Combined Human-Exoskeleton MSC.Adams model of Upper body's CoM is a lump model of the human's upper body with both mass and inertia values. Furthermore, passive joints are not visually represented in this model.

between the foot and floor. The foot was modeled using a rectangular box shape. Contrary to the parametric model of the dynamic model, foot sizes were adjusted with respect to the tallest human case. Constant foot size for all three cases was used as this is a common modelling approach in the literature [35]. The ground was represented by a flat rigid surface. Depending on the level of penetration between the geometries of foot and floor, the contact force was calculated as follows,

$$F = kx^e - \dot{x}c_{max}u(x), \tag{12}$$

where k is the stiffness representing the contact stiffness, x is the penetration between the geometries of foot and floor, c_{max} is the maximum damping coefficient and d is the penetration at which the maximum damping is applied, $u(x)$ is a step function. The parameter force exponent e,defines the force deformation characteristics. Values of $e > 1$ are used to represent increasing stiffness with the penetration depth, while

$e < 1$ is used where the contact force decreases with penetration. The value of $e = 1$ represents a linear spring. In the model, the contact parameters are chosen as: $k = 1.0E + 006\ N/m$, $e = 1$, $c_{max} = 1.0E + 004\ Ns/m$, $d = 0.1\ mm$.

3.1.2 Stiffness Optimization

An optimization study was performed to find the optimum value of the stiffness of the ankle. The objective function was chosen so as to minimize the integral of the absolute value of ZMP. An additional parameter was added to the objective function in order to penalize conditions when there is no contact between the foot and the ground. The objective function is shown as follows,

$$f = min(\int_{t=0}^{T} (|Y_{ZMP}| + P)dt), \tag{13}$$

where Y_{ZMP} is the momentary ZMP value of the system and the P is the penalty value. To set the penalty value, the resultant ZMP values were sampled with different stiffness values K, and the maximum momentary ZMP value was chosen as the current penalty value.

$$1000 < K_{pas} < 5000 \tag{14}$$

The lower and upper bounds were found by performing several simulations prior to optimization runs to make sure that it covers the range of the ankle. More specifically, a variety of different K_{pas} values were simulated. After a careful investigation of the simulation results by trying random K values, it is concluded that with lower K values the human/exoskeleton model tips over laterally towards the sway direction. On the contrary, for higher K values, the system bounces back and tips toward the opposite direction of the motion.

If the optimization converges to either lower or to upper values, then the boundaries were defined to cover a wider range and the optimization was re-run.

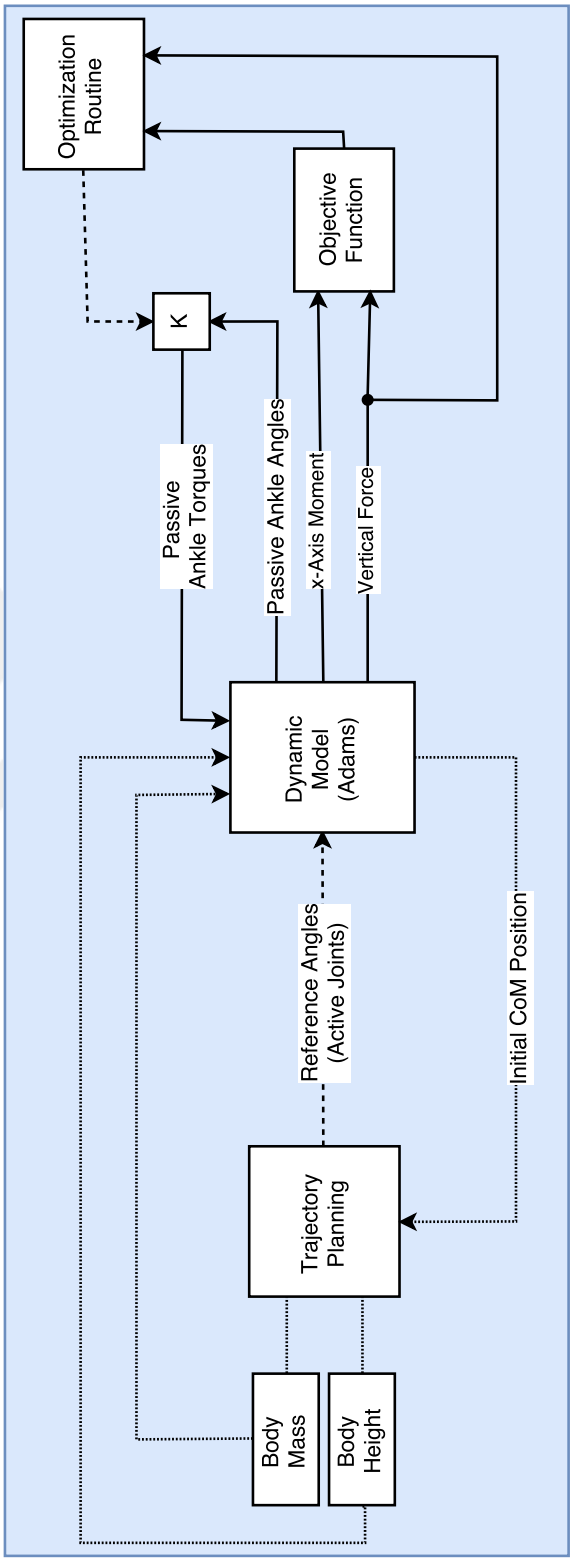

Figure 28: Workflow of the optimization model

Simulinks Response Optimization toolbox was used for the optimization study. MSC.ADAMS was used as the solver. Simulink/ADAMS co-simulation with interactive option was performed for the numerical integration and calculation of the objective function. Sequential Quadratic Programming (SQP), a gradient descent based algorithm, was selected as the optimization algorithm. Tolerances on the constraints and objective function were set to 0.001. Maximum iteration number was set to 100. During the optimization solution phase, the objective function was monitored for each iteration to make sure that the optimization converges.

3.1.3 Sway Trajectory Generation

Reference joint angle trajectory were generated via a prioritization-based Inverse Kinematics (IK) algorithm that considered only the 8 active joints [38, 39]. As an example, HA/A and BCM trajectory references are displayed in Fig. 29.

Since the two predetermined passive joints are locked, the generated IK solution uses only 8-DOF to control BCM. The MSC.ADAMS-MATLAB co-simulation model takes into account the flexibility in the ankle joint, which was considered as perfectly rigid in the reference joint angle trajectory generation phase.

The proposed methodology was applied to the models with different body weight and height as part of various case studies. Three case studies are summarized in Table 5.

Table 5: Parameters for three cases

Cases		1	2	3
Body Height	cm	190	175	160
Body Weight	kg	100	80	65
Total Weight	kg	138	118	103
CoM Height	cm	91.1	86.2	82.3

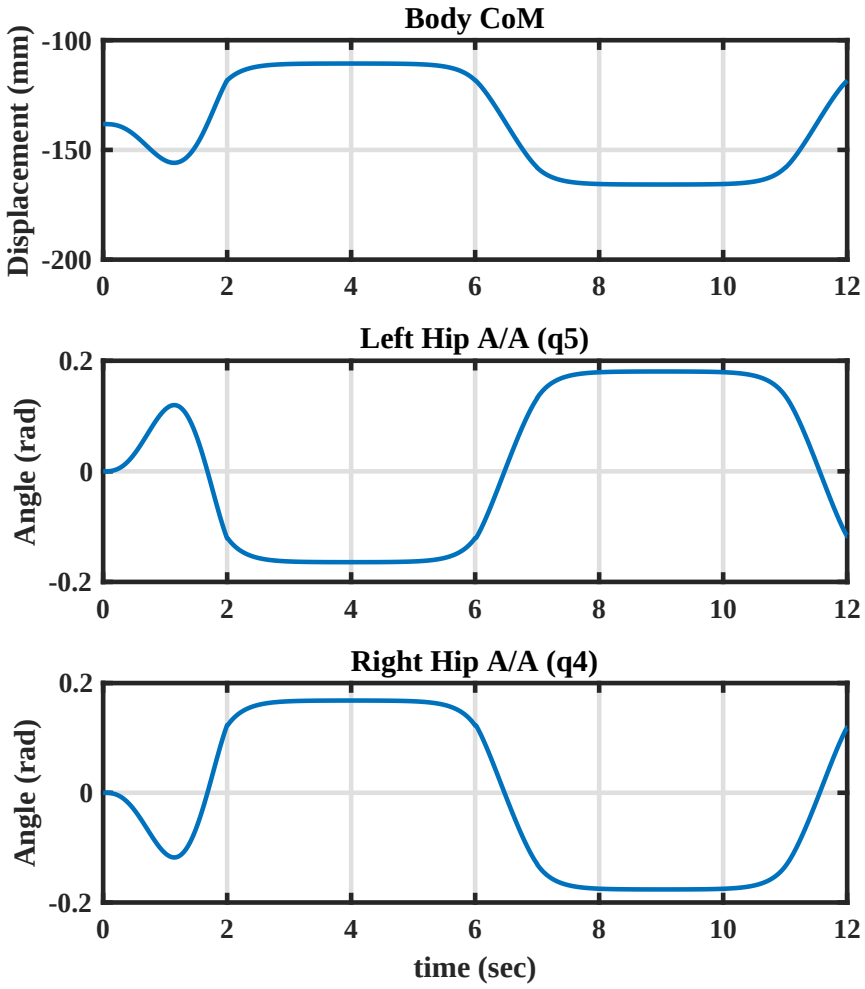

Figure 29: HA/A angles and BCM position of the generated sway trajectory (top) BCM position with respect to left foot (middle), left hip (bottom), right hip

3.1.4 Results

The optimization is first applied to Case 1. For the initial value of the stiffness K_{pas} = 2000 Nm/rad was chosen. The optimization converged to an optimum value of $Kopt$ = 4701 Nm/rad after 6 iterations and 36 subiterations. The convergence of the stiffness as a function of iterations and subiterations is shown in Fig. 30.

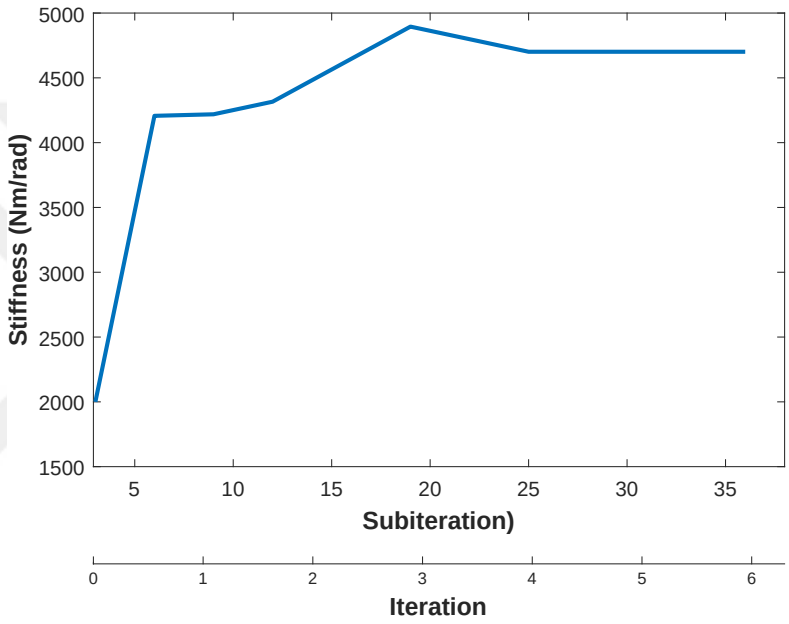

Figure 30: Stiffness vs. optimization iteration (subiteration) for initial case

In Fig. 31, the response of the passive joints with different stiffness values are given with the optimized stiffness value of 4701 Nm/rad for Case 1. Initial value of K_{pas} = 5500 Nm/rad, a considerably high stiffness value, it is observed that the models foot lose its contact from the ground. Therefore, a penalization is added to the objective function in accordance with (13). This could be seen from the step increases on the time response of the system shown in Fig. 31. Contrarily, the objective function values which are lower than the general trend of the same graph are the result of the impact when the foot hits the ground. The impact to ground results in higher forces on the foot, x-axis moment is constant. For relatively lower K values (3000Nm/rad

and 4000 Nm/rad) even the ZMP values get closer to an almost constant range; the variation of the response was reduce as K value reaches to the optimum value of 4701 Nm/rad.

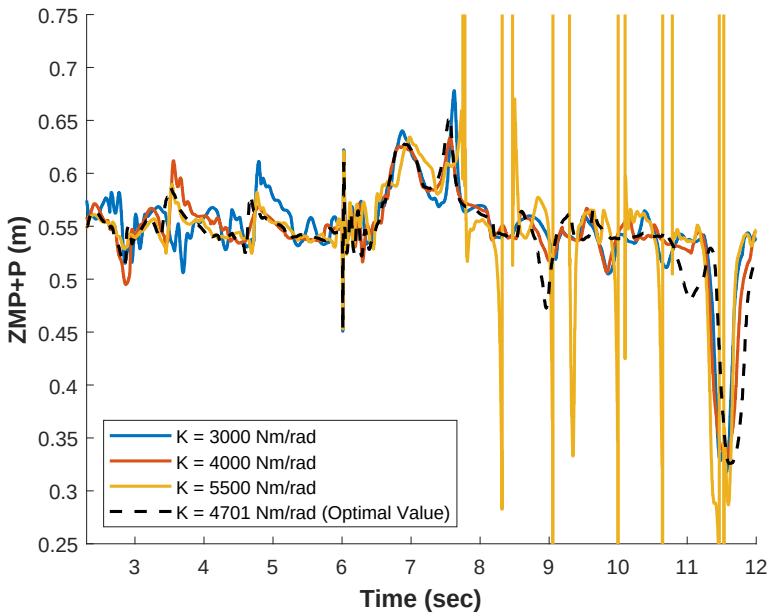

Figure 31: Comparison of objective function results with different stiffness (K) values

The algorithm was then applied to the other two case studies. Similar convergence results in terms of the number of the iterations as the first case study were obtained, and therefore the results were not plotted for the sake of conciseness. The optimum stiffness values for three case studies summarized in Table 5 are 4701 Nm/rad, 2134 Nm/rad, and 697 Nm/rad for Case 1, Case 2 and Case 3, respectively. In Fig. 32 the angular deflection of the AI/E joints with different stiffness values are plotted with respect to time.

3.1.5 Discussion

In this chapter, a lateral swaying motion was considered since the passive joints are most effective in the plane of swaying motion. The forces created by the active hip joints during sway motion can be balanced with the help of AI/E joints. For more

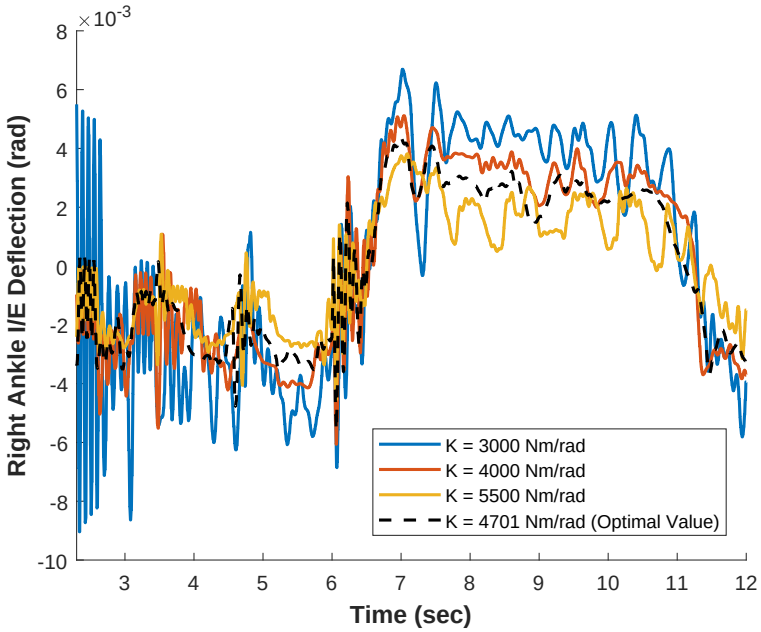

Figure 32: Comparison of Right AI/E deflection values with different stiffness values

complex motion like walking, loads on the passive ankle joints can be due to a much more complicated dynamics interactions. That being said, the motion of the passive ankles is more dominant during lateral swaying motion than walking due to support by both feet compared to one foot raised during walking [95].

Losing the balance of the system under swaying is of great concern, which is only possible when the active joints can not track the desired motion under external disturbances. One possible example of losing the balance is due to low ankle stiffness where the system may fall sideways. It is important to observe the higher oscillation amplitudes corresponding to lower and higher stiffness values compared to the much lower oscillations for the optimal stiffness value. The results suggest that the stiffness should be carefully engineered to minimize oscillations during 3D walking and similar dynamic conditions.

The simulation results show that the optimum K value change with respect to body mass and body height of the human. Further simulations are acknowledged as

future work in order to quantify the relation between the mass/height of the system. Since these parameters are affected by more than 28 different parameters of the human body and the exoskeleton, this study was acknowledged as a future work.

3.2 Mechanical Design

After the simulation study is finalized, realization of such a system was the next step. As mentioned in the Chapter 2, a parametric spring topology is created. Even though this topology can be adjusted for different stiffness values, since simulation and experimental values always have some error margin, a fully adjustable spring system seemed more suitable for the case.

Considering linearity snd wide range of adjustability, linear springs deemed more suitable [73]. The basic design was using two linear spring as a couple to each other with a cam mechanism to create the necessary torque for the passive joint [96]. Relation between the linear stiffness of the spring and the rotational stiffness is given in (17),

$$k_s \theta_{ank} = \tau_{ank}, \tag{15}$$

$$k_l x_{max} d_0 = \tau_{ank}, \tag{16}$$

$$\frac{k_l x_{max} d_0}{tan^{-1}(\frac{x_{max}}{d_0})}, \tag{17}$$

where k_s is torsional spring constant, k_l is linear spring constant, θ_{ank} is the maximum allowable ankle angle, x_{max} maximum length of spring deflection, d_0 is the distance between the ankle joint axis and the spring. However this relation is solely based on the constant d_0 value which will be addressed with a CAM-like-mechanism. As

may be seen in the Fig. 33 this fundamental structure was modelled in MSC.Adams environment. System designed with 2 linear springs on each side of the ankle, and calculations were made according to this system. In accordance with the results of simulations, with using only two linear springs, desired values in a range found in Section 3.1.4 are impossible to realize, while containing the size of the system. Yet, this simulation also showed the validation of the (17).

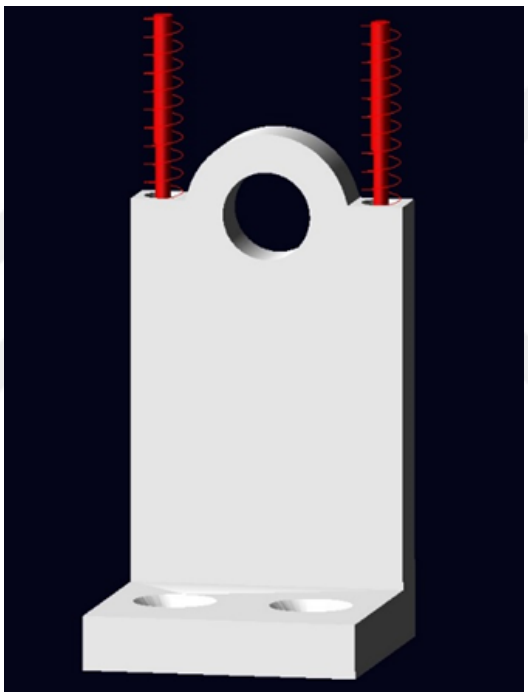

Figure 33: Simulation model for Case 1 in MSC.Adams environment

After repeating the calculations and validating them via simulation while considering various designs, it was understood that it is not possible to realize the desired adjustable stiffness value without exceeding the system boundaries. Thus, while staying in the boundaries, the highest torsional spring constant was aimed by using off-the-shelf manufacturable linear spring values. Hence, angle limitation is held on ± 10 degrees of angle maximum. After various number of springs and spring types combination, a system is designed with the total number of eight springs whose information is given in the Table 6. With these combination, a $1.4 kNm/rad$ stiffness

is realized.

Table 6: Properties of linear springs

Property	Unit	Spring-A	Spring-B
Outer Diameter	mm	22.5	20.5
Free Length	mm	48	52
Max. Deflection	mm	6.5	10.5
Number of Coils	-	8.5	9
Wire Diameter	mm	5	4
Stiffness	N/mm	165.081	91.560

After the initial requirements for the passive joint such as, spring dimensions, number, and placements, are decided mechanical design of the foot with passive I/E joint is designed. For the purpose of adjustability springs are preloaded. This preload can be adjusted with a single screw. Designed system for the passive joint can be seen in Appendix C.

CHAPTER IV

LOWER BODY EXOSKELETON DESIGN

Design of an exoskeleton is a complex engineering problem. As mentioned in the Section 1.1.1 safety is always the first concern, it is because of the fact that the exoskeleton is worn by a human subject.

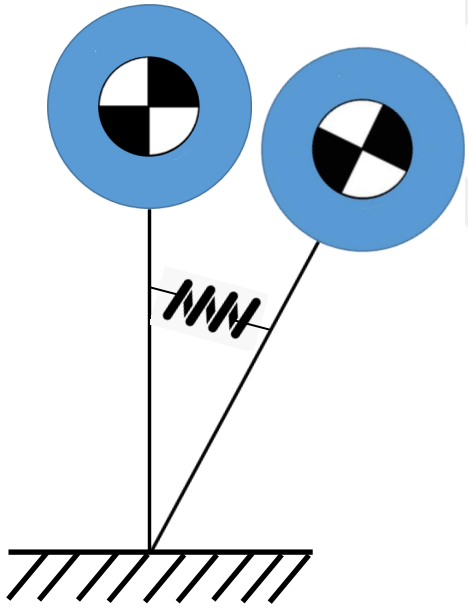

Figure 34: Simplified version of the human-exoskeleton physical interaction

The idea of the inverted pendulum simplification for the bipedal robots has been studied in the literature [97] for a long time, and is used in the locomotion of various robots. Due to multi-dimensionality, discontinuous contacts, and uncertainties associated with the exact dynamic models of bipedal robots, researchers often use reduced-order abstracted models that encapsulate the dominant characteristics of the system. In these models, the whole body is represented as a single body that is attached to the ground via a massless telescopic leg [97–99]. Therefore, if the real

physical system mass is accumulated around the upper torso, these approximations can represent the dynamic system behaviour with respectively more accurate, compared to the case of robots with distributed mass [100]. A recent bipedal design "Cassie" by Agility Robotics is a specific application of this simplification method to a robot design [101, 102]. They adopted this pendulum like structure by taking the knee flexion actuator to hip level and the toe (ankle) joint actuator to knee level, and connecting all these transferred actuator with a four-bar-linkage. This actuator design is also implemented in other systems like WALK-MAN to reduce the leg inertia [103].

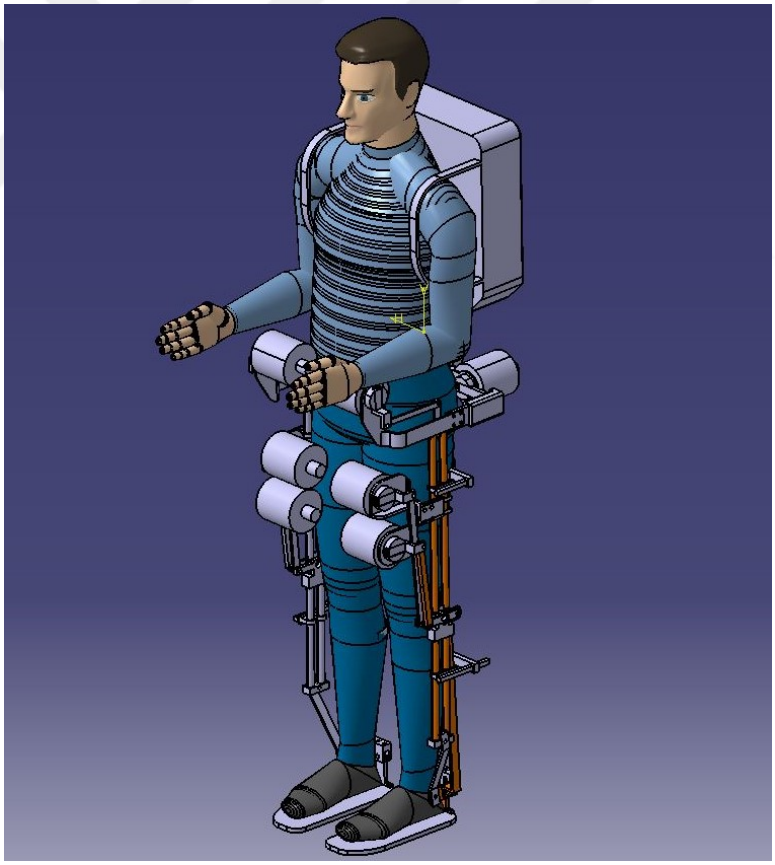

Figure 35: First conceptual design of the exoskeleton

One one hand, when the inverted pendulum simplification is considered from the lower body exoskeleton perspective, human and the exoskeleton can be seen as a

single lumped pendulum-like structure. On the other hand, an exoskeleton design with enhanced multi-state sensing ability, can allow this system to be simplified as two independent pendulums, which are connected to a stiff structure, see Fig. 34. In the light of these facts, it is of crucial importance to develop a lower limb exoskeleton with relatively light-weight legs and with concentrated mass on the hip level of the human. This configuration is a unique part of the design compared to these from the literature. This proposed design idea is shown in Fig. 35.

4.1 Design Requirements

A literature search was performed to determine the design requirements. However, no consistent information were found regarding the proposed design. Therefore, numerical simulations were performed to identify the necessary design requirements.

For the design of the limbs, a simulation were co-simulated using MATLAB and MSC.Adams software. Details of this system can be found in Section 3.1.1.1. A human, whose height and weight values are $1.90m$ and $90kg$, respectively, was placed with a exoskeleton concept which was created using CAD software. Human-robot model is simulated for the half of a regular person's walking frequency ($\approx 3Hz$). Thus, the maximum velocities at the joints have been set to $9.55rad/s$, and the forces were gathered according to this maximum value.

Table 7: Joint loads from simulation results

Forces	Ankle Roll	Ankle Pitch	Knee Pitch	Hip Roll	Hip Pitch
Sagittal Axis (kN)	0.15	0.15	0.15	0.15	0.15
Frontal Axis (kN)	2.00	2.00	2.00	1.50	1.50
Transverse Axis (kN)	0.35	0.35	0.35	0.40	0.4

Adjustable limb was an important feature of the design to consider. Thus, the literature has been reviewed to determine the required limb dimensions, especially, for the thigh and the shank [104]. To define an arbitrary limit for these dimensions,

both female and male subjects were chosen to collect data on their height. Limb length dimensions can be seen in Table 8.

Table 8: Link lengths of human

	Heigth (m)	Thigh (mm)	Shank (mm)
Male	1.90	459	473
	1.60	387	398
	Heigth (m)	Thigh (mm)	Shank (mm)
Female	1.80	380	448
	1.50	316	373

Final requirement for the design was the angle range of each specific joint. First strategy to define these values were to investigate the required angle limit for the 3-D walking support. By considering the all possible motions (sit to stand, step etc.) which can be done by an healthy subject, the existing data in the literature was used initially.

Table 9: Joint Limits

Joints	Maximum		Minimum	
	Human	Exoskeleton	Human	Exoskeleton
HA/A	30°	20°	−45°	−20°
HF/E	100°	18°	−25°	−18°
KF/E	90°	80°	−5°	0°
AF/D	45°	20°	−20°	−20°
AI/E	30°	10°	−20°	−10°

4.2 Exoskeleton Body Structure

To define the link structure of the exoskeleton, different proposed systems in literature were studied. One structure came one step forward; Bartenbach et al. suggested a two hollow carbon-fibre centred design in [87]. In this design, designers considered adjustability of the different links of the robot with respect to the size of the human limbs. Additionally, it was observed that designers used similar joint structures for each link. Even though this strategy creates many advantages, especially for manufacturing and maintenance, since each joint has unique needs, such a strategy can

lead to overly safe designs. Hence, by considering features like adjustability, joint sequence, and manufacturability, two tube design without the further joint design was selected for the base of our lower body exoskeleton. As seen in Fig. 35 this link structure is combined with our inverted pendulum based design approach.

4.2.1 Bearing Selection

Based on the concept design, a manufacturable design was initiated by focusing the selection on the right bearing. In the bearing selection procedure, the most vulnerable joint of the robot was used as the selection criterion. The worst possible scenario for each joint was calculated using the F_x and F_y values: see Table 7 and (19). By considering the maintenance factor, bearing chosen for the most critical joint was also used in the other joints. In each joint, connection of two links was done in a male-female part structure. An example from the knee joint can be seen in Figure 36. This structure provides two advantages; **i)** since the axial loads are divided into two equal parts, bearings with smaller diameters could be used. **ii)** with this structure, undesired bending moment created by the distance between human leg's CoM and the bearing center was transferred to the structural elements.

Bearing selection was done in accordance with the method given in [105] for limited life-cycled bearings. Approximate maintenance life for the design was chosen as one full year. However, considering the fact that possible daily usage of a regular user is less than 24 hours per day, it is possible that the actual potential life is much longer than one year. Load rating (C_{10}) of the desired bearing was calculated for this given life time and maximum possible load value with a stochastic 1.5 safety factor.

$$x_D = \frac{L_D}{L_R} = \frac{L_d n_d 60}{L_R} \tag{18}$$

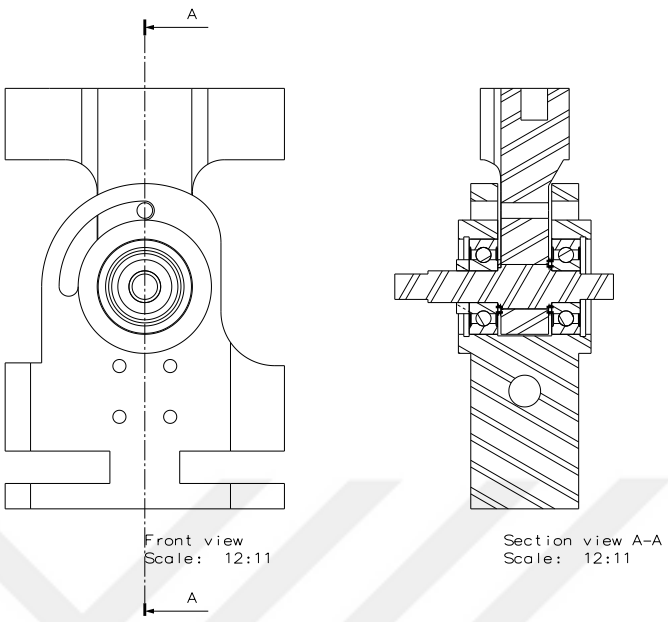

Figure 36: As an example to exoskeleton joint structure, v1.0's knee joint

$$C_{10} = a_f F_d \left[\frac{x_D}{x_0 + (\theta - x_0) log(\frac{1}{R_d})^{1/b}} \right]^{1/a} \tag{19}$$

the selected parameters in (18) and (19) can be seen in Table 10

Table 10: Bearing selection parameters

Parameter	**Multiple of Rating Life**	**Desired Life**	**Rating Life**	**Desired Speed**
Symbol	x_D	L_D	L_R	n_D
Unit	-	years	rev	rad/s
Value	-	1.50	10^6	9.55
Parameter	**Application Factor**	**Weibull Parameters**	**Reliability Contour**	
Symbol	a_f	x_0, θ, b	R_D	a
Unit				
Value	1.2	0.02, 4.459, 1.483	0.95	3

From (19) load rating was calculated iteratively as app. 4 kN. In accordance with this value, bearing with code 6200-2Z[1] was chosen. After this selection one further

[1]https://www.skf.com/group/products/bearings-units-housings/ball-bearings/deep-groove-ball-bearings/deep-groove-ball-bearings/index.html?designation=6200-2Z

calculation was made to predict to approximate lifetime of the bearing.

$$F_e = (X_i V F_d) + (Y_i F_a) \tag{20}$$

$$L_{10} = \frac{rev}{60 n_d} (\frac{C_{10}}{F_e})^a \tag{21}$$

By using the relation in (21) an approximate life of the bearing is calcualted as $1.5 years$ which was 50% higher than the initial assumption.

4.2.2 Link Design

Another challenge with the design is to determine the connection strategy between the aluminium and the carbon-fibre members. Main reason for this connection structure becoming a problem is hidden in the structure of the carbon-fibre. Carbon-fibre members were produced with a procedure called filament winding, these members shows high durability in their initial form. However additional interventions on the members break the fibre structure, thus any product-life prediction and safety calculation loses its accuracy. Since this unpredictable life expectancy creates high risks, a connection method which does not require an additional interventions on the members had to be chosen, therefore commonly used epoxy adhesive was applied to use while connecting the members. On the contrary, this also creates another issue; in a case of a modification or miscalculation, usage of adhesive may cause to a member loss. By considering these possibilities, additional expendable members are manufactured which act as connectors between main aluminium members and the carbon-fibre members.

4.2.3 Adjustability

Adjustability of the links was another important issue. At this point, two tube system suggested by [87] provides a sufficient capability for the design. Designing two-main

Figure 37: Additional expendable members designed to connect carbon-fibre members with aluminium members as placed on carbon-fibre tube

carbon-fibre tubes are sufficient enough to carry axial load created by the mass and the impact from the ground, as well as sufficient to carry the bending moments. Moreover, telescopic tubes allow me to change the size of the links. Bartenbach et al. used a clamp mechanism to put a constraint to the adjustable links [106]. However, our experiments showed that initial design was not sufficient due to the poor manufacturing quality.

Experimentation was done with the three cases shown in the Fig. 38. In the first trial setup a two tube structure were experienced with a single clamp to adjust the connection. For the worst case scenario, a single tube was loaded with a 100 kg compression. Unfortunately, the structure was unable to support to load and failed. This first experimental structure can be seen in Fig. 38(A). After a careful investigation, it is concluded that coefficient of friction between two carbon-fibre tube was not sufficient. At this point the only solution was the increase the clamping force. On the other hand, even the tube wall thickness was sufficient for the design shear forces and the bending moments created by the actuators and the pilot, was not

sufficient for an extra clamping force. To improve that, an additional second clamp was designed and connected to the first clamp with a rigid link as seen in the Fig. 38 (B), the different strategy with this to benefit the higher friction coefficient between the aluminium and the carbon-fibre.

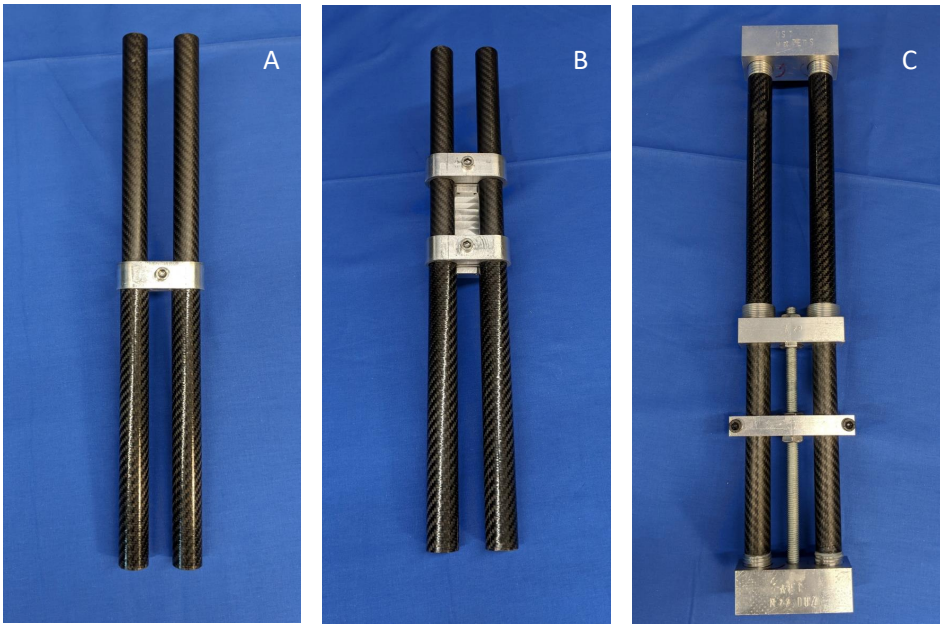

Figure 38: Chronological experiment setup for the adjustable link structure (A) First version with a single clamp, (B) Second version with double clamp structure and finally (C) Final version with a power lead screw

The second clamp was attached to the lower carbon-fibre tube to squeeze it. Even though the design showed improvements, still a load of 80 kg per tube was greater than the maximum allowable boundary. At last, this led me to the final design. In the final design, an extra power screw is added to the system, to carry the axial load. In the final design,as different than the first two design strategies, axial load was transferred between the joints with the help of a screw through the upper tube. For the realization of this hypothesis, an experimental structure in Fig. 38 (C) was manufactured. Like in the second case an additional clamp was added to system in case of insufficient load carrying via the upper carbon-fibre tube. It was because of

the contrary of the first two case tube was transferring the load with a highly small surface area as pure axial stress. With a static safety factor of 12, an M10 screw is selected as the connection screw and the system was designed accordingly. In this final attempt, the structure was sufficient to hold the adjusted link in the position without the possible use of the second clamp. Additional to success on the load carrying, this new design also extinguish the possible failure risk, which may cause by the changing of the friction coefficient change caused by the temperature change, unpredicted shape deformation etc.

4.2.4 Joint Design

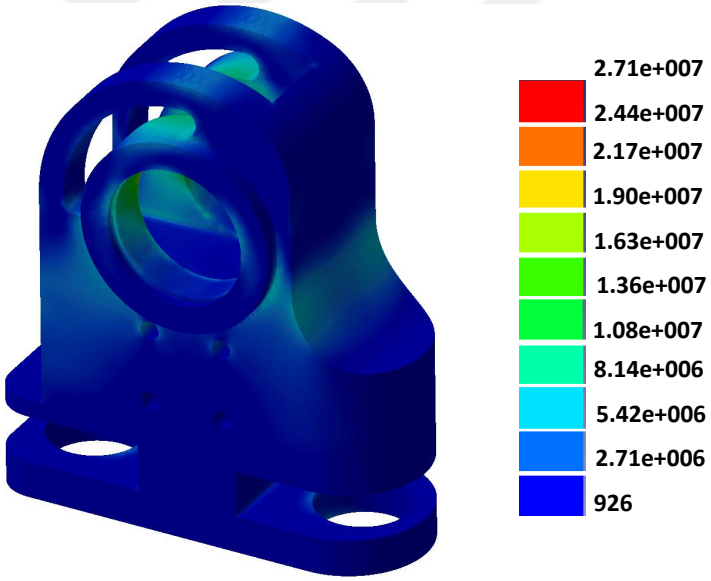

Figure 39: FEA example for a joint, under pure compression

Having determined the connection strategy, I have proceeded toward the joint design. Bearing size, diameters of the carbon-fibre tubes, and the power transmission strategy, (see Section 4.3), played prominent role in the shape of the joint structures. As the second priority, manufacturability and the cost of the manufacturability affect the shape of the structures. It must be mentioned that these geometrical and cost limitations let the joint system to be over safe.

4.3 Power Transmission

Inverted pendulum structure of the exoskeleton caused new design challenges, in particular transmission of the power from actuator to its related joint. However robots and exoskeletons like use rigid four-bar-mechanism and exoskeletons like use rigid five-bar-mechanisms to transfer motion [101, 103, 107]. Rigidity must be the key component at this point, since the designed system lean on the elastic actuators power transmission with relatively soft power transmitters like belts and chains could eventually affect the compliance of the system. Because of these reasons, already suggested [34, 108] structures were not preferred.

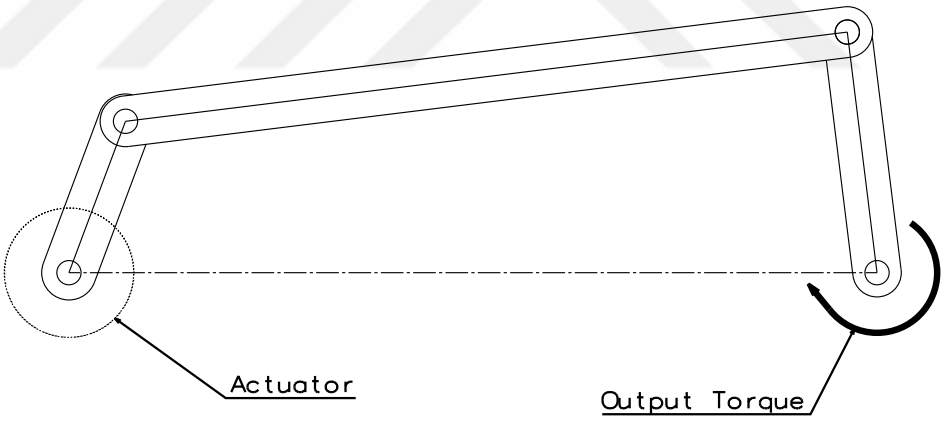

Figure 40: Four bar

On the contrary, this structure brought a possible opportunity for the torque tranmission gain. This investigation was done in this method: a simulation on MATLAB environment was developed with parameters of four-bar's link sizes, initial angle of the actuator and the joint. With this tool, resultant torque values were observed under input angle change with a constant input torque. In parallel to this simulation,

another simulation was also developed in MSC.Adams environment. Same parameters were also applied to this simulation. However, in MSC.Adams output torque reading became an issue and the main reason for this was that the MSC.Adams is missing a shaft to shaft torque sensor. This problem was not resolved, thus a comparison between MATLAB and Adams simulations were done based on static results. Since the study was completed in the pre-design period, inertia terms were not considered This also reduced the possible error between two solutions. A spring with high stiffness was modelled in the output joint, such that given input with minimum deflection reaction of this spring provided the output torque.

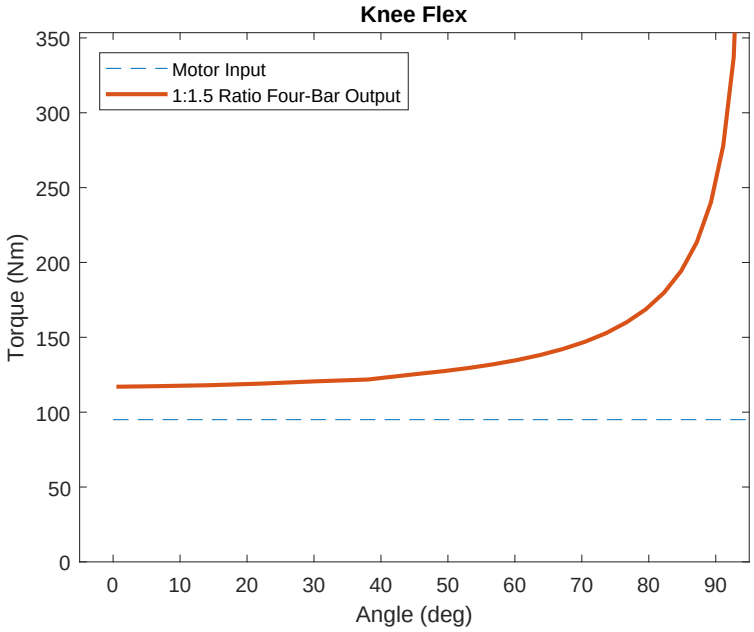

Figure 41: Simulation result for the possible gain for a four-bar mechanism with crank/coupler ratio of 1.5

4.4 Braces and Rings

The alignment between the mechanical limbs, and the user's limbs is a key to successful exoskeleton operation. The most reliable way to achieve this alignment is to attach the robot and the actual limbs with orthosis limbs by keeping the degrees of

freedom between those two in mind.

It is important to take into account that the connection between the robot and the human needs to be secure with a high grip since the user profile of this device is the individuals with lower body paralysis. Many exoskeleton designs, which address these points, can be found worldwide in the literature [33, 34, 109]. All referenced systems were developed for patients that suffer from paraplegia. These systems use similar approaches to the proposed exoskeleton regarding human-robot attachment equipment. The proposed design can be found in Fig. 42.

In general, orthosis molds are made of polyethylene, polypropylene, and polycarbonate, but in some cases, lighter materials such as aluminum can also be used. Due to their flexibility, plastic and its derivatives are the most preferred materials for that kind of equipment. The types of plastic components differ from application to application. Table 11 summarizes the relationship between plastic types and the application.

Table 11: Qualitative comparison of the possible mold materials

	Polyethylene	**Polypropylene**	**Polycarbonate**
Stiffness	Soft	Soft	Rigid
Shape Adjustability	Yes	Yes	Non
Durability	Low	Average	High
Manufacturing Type	Firing	Firing	Vacuum drying
Density	Low	High	High

As shown in Table 11, the orthosis made of polyethylene and polypropylene have less rigidity than these made of polycarbonate. For this reason, they are more elastic and adjustable for different limb sizes. These materials are also less durable. However, this does not pose any risk for the user; even it eases the attachment procedure. Vacuumed members are more effective when compared to their counterparts heat-treated. The downside of those members is that they are manufactured just for one individual with specific dimensions. Lighter molds decrease the required torque at a joint, so they are suitable to deploy in a project like this. When all those points are

examined, polyethylene orthosis attachments are the most advantageous ones.

This issue is generally realized by adjusting the length of the robotic limb by changing the position of the orthosis apparatus concerning the subject's lower and upper leg positions. These adjustments make it possible, one exoskeleton to be worn by different individuals with different body measurements. Most exoskeletons utilize this adjustment principle, but it is also possible to achieve customizability in accordance with the thickness and the distance between the limbs on sagittal/coronal planes. This approach increases the number of people, that can use the exoskeletons. Hora et al. discussed the domain of the position adjustment in their work and their measurements confirm that its possible to use the same exoskeleton for a woman and man, who is $1.55m$ and $1.90m$, respectively [104] .

The manufactured exoskeleton is composed of an orthosis apparatus for upper and lower legs and a corset to surround the back and the hips. The orthosis apparatus are covered with neoprene material to minimize the deformations on the subject's skin. Upper and the lower legs have orthosis apparatus with a half circle shape that leaves open the inner side of the leg, which is directed to the sagittal plane. In this way, the equipment can help the patient to preserve his/her balance while providing a posture that may enable a natural and comfortable walk pattern. The orthosis apparatus can be tightened by strips through the dedicated gaps for them. Adjustments in sagittal, coronal planes and height can be made using the integration of three different sliding units. The system is shown in Fig. 42. Similar strategies can be seen in [35, 106, 110]

The sliding units are present in both upper and the lower parts of the leg. The height adjustment in Z-axis enables the system to be adjusted for an individual position by considering the exoskeleton's height. In Y-axis, it is aimed to attach the individual to the system by taking individual's leg and hip measurements into account. On the other hand, the same aim is pursued in the X-axis by making adjustments according to the leg spread and thickness. The sliding unit in the X-axis is positioned

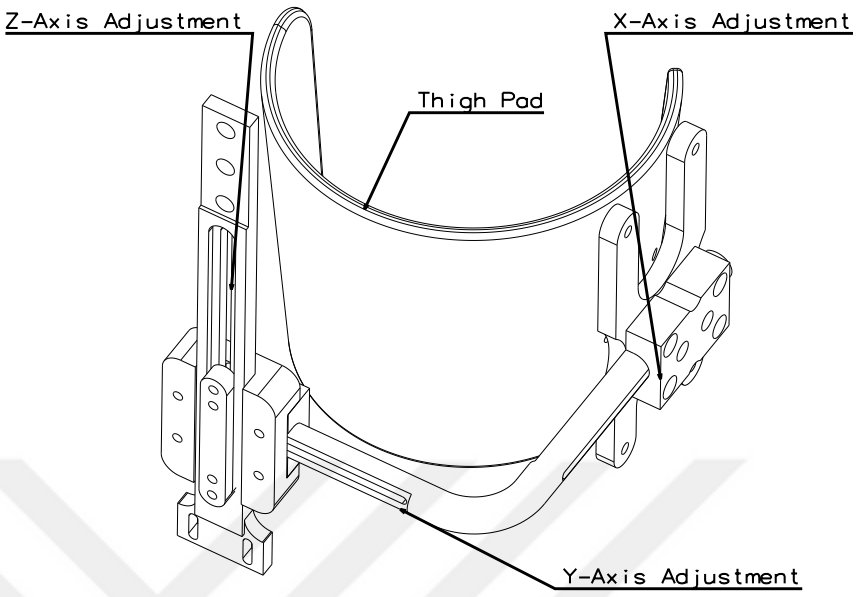

Figure 42: Thigh pad position adjustment system, distance between the upper thigh can be adjust in three axes (x, y, and z)

in the back of the leg, where the orthosis apparatus is also attached. The sliding units limits were calculated, using the work that de Hora et al. published. All limitations were considered in a margin of error of $\pm 15\%$.

4.5 Manufacturing of the Exoskeleton

The exoskeleton manufacturing process can be examined in three stages: **i)** the procurement and integration of auxiliary members, **ii)** machining of the designed members, **iii)** integration of the actuators presented in Chapter 2 into the system.

In the first stage, the members, which are neither designed nor manufactured by the author, were chosen and some additional members were designed to append these members to the rest of the system. The commercial off-the-shelf products used in the design are as follows:

- The foot attachment apparatus, which is standard equipment that is used to

attach snowboards to individuals. This choice has been made based on communication with EPFL's M.Bouri. This apparatus ensured that the attachment of the person the exoskeleton is safe and quick. However, it also introduced additional undesired weight to the system. Thus it was replaced with a design that only uses attachment strips.

- For the attachment of the legs, the apparatus, which were mentioned previously in Section 4.4, were manufactured in a way that their dimensions are adjustable. All equipment are mounted to the robot using four screws, which makes any member to be easily replaced in a condition that they may underperform.

The matters that are handled in the second stage can be grouped as the following:

- As stated in the design part, to decrease the weight and achieve the customizable structure, the limbs of the robot have been manufactured using carbon-fibre pipes. A detailed prototype limb has been machined to investigate the further aspects of the design and to prove that the system can deliver the specifications as well as. Fig. 38(C) displays the prototype.

- As mentioned in the previous Section 4.3, actuators taht power the KF/E and AF/D joints placed near to hip. Due to this position change, four bar mechanism are designed for these joints. In a similar manner actuators in the hip region are replaced in order to resolve any conflict with the individual's arms motion. After those replacements, the distance between the actuator and its dedicated joint has increased. To solve this issue, four-bar mechanisms utilized to transfer the motion from the actuator to the joint. Similar to the case in adjustable limb dimensions, these four-bar mechanisms are also customizable with reverse-threaded screws. Even though turnbuckle equipment are readily available in the market, standard equipments were not sufficient in terms of the adjustability. Thus these members were custom built.

- The aluminium members, which are machined, are combined with their carbon-fibre counterparts using Loctite EA 96466. The carbon-fibre members are designed to have a thickness of $1mm$, where the male and female members have an outer diameter of 18 mm and 22 mm, respectively. These dimensions are used in the prototype that is shown in Appendix A.

- Members were produced with three main manufacturing techniques, tuning (with Computer Numeric Control (CNC) Lathe), milling (with CNC Milling Machine), and laser cut. By concerning the overall budget each member was manufactured with same series of aluminium except for the joint shafts, which were made from stainless steel.

Some of the members could not have been manufactured due to ergonomic concerns. These parts were replaced with their 3D printed replicas until a more viable solution is found. The main concerns for each part can be listed as follows:

- The part that transmits ankle actuation to the knee: the investigation on joint limits continues.

- Attachment of the knee actuator to the knee: the current position of the part may create inconvenience to the user.

- Passive wrist joint spring holder box: its effect on the user ergonomy is being tested.

- Intermediate parts for body attachment: Its performance on different users for further investigation.

Finalized design and manufactured prototype can be seen in Appendix B.

CHAPTER V

CONCLUSION

In this study, the design and the development of a lower body exoskeleton is presented. Conclusions, from this research are summarized as follows:

- An integrated design approach for an SEA was proposed by focusing on stiffness tuning and fatigue analysis of the elastic element. A variety of the spring topologies were experienced to find a parametric topology, where stress distribution and stiffness limits were the main objectives of this topology study. By using a novel 2-spoke spring topology, the stiffness was formulated via extensive computational analysis. Furthermore, two different design parameters (ST and FT) were chosen to parametrize the spring design. To this end, 52 spring models with distinct ST and FT values were simulated as a part of the parametrization. The results from the simulation study was utilized to fit an empirical equation that allows me to get springs to meet different application scenarios. An empirical equation of the quadratic form was fitted to the simulation results by following a least-squares approach. The quality of the empirical model is tested on four additional design with excellent correlation. The accuracy of the spring design was verified with the stiffness, break-up, and strain rate tests on TTM. Thermal performance of the SEA was also verified via experimental methods. The results indicate that the actuator is suitable for physical human-robot interaction scenarios and can be reliably employed power to robotic systems for long-term and repetitive use. The finalized version of the actuator and the elastic component is tested for controllability. This finalized topology has also satisfied a fatigue requirement, with the result of the analysis minor changes

have been done on the design, and the final grade of material is chosen.

- A passive joint stiffness optimization was performed to find the optimum stiffness value, which can adequately provide the required hip motion and still support the overall weight of the system. The sway motion simulation results from the three case studies considered indicate that optimization depends on many factors such as the COM of the human/exoskeleton system and the weight of the system. Since an adjustable exoskeleton is used for the model, mass and inertia of the exoskeleton become more dominant for a short user. In addition, the effect of other parameters such as single limb length, mass ratio of torso, etc. can be investigated. In this study, a generic human body mass and inertia distribution based on healthy human population was used. However, body mass distribution of a paraplegic patient can be quite different compared to a healthy human. The analysis and the optimization of the system with body mass, inertia, and height values of paraplegic patients via experimental investigations are acknowledged as future work.

- A novel flywheel like exoskeleton is designed to get a better stability by using the structural elements. Four active DOF per leg combination chosen for crutchless 3D walking support. Link structure of the exoskeleton was designed as adjustable by considering the needs of the possible users. This suggested design also helped us to gather electronics close to backpack where the batteries and the CPUs will be placed. Final design of the exoskeleton weights app. 42kg (without the batteries) which can be improved in next versions.

APPENDIX A

VERSION 1.0 EXOSKELETON

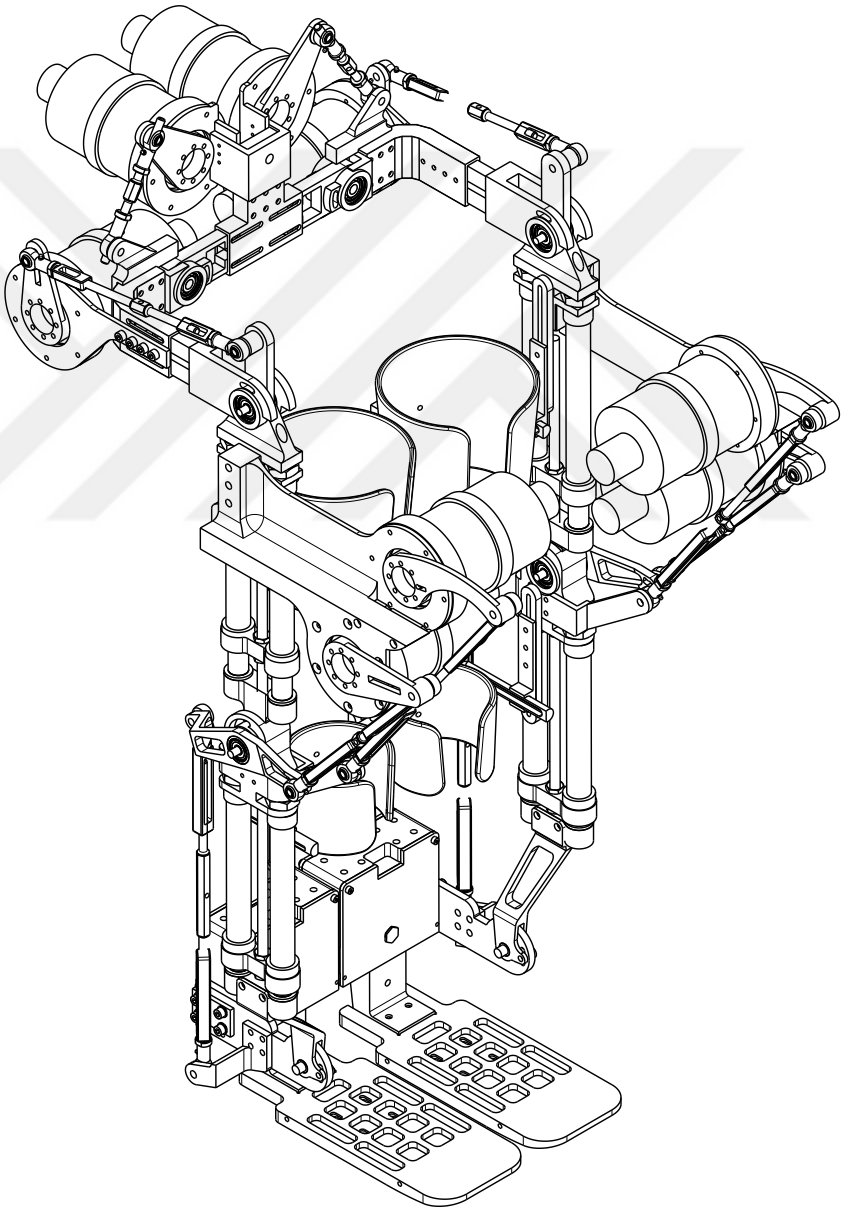

Figure 43: Final design version 1.0

Figure 44: Manufactured version 1.0 with mock actuators, on a healthy female subject

APPENDIX B

VERSION 1.1 EXOSKELETON

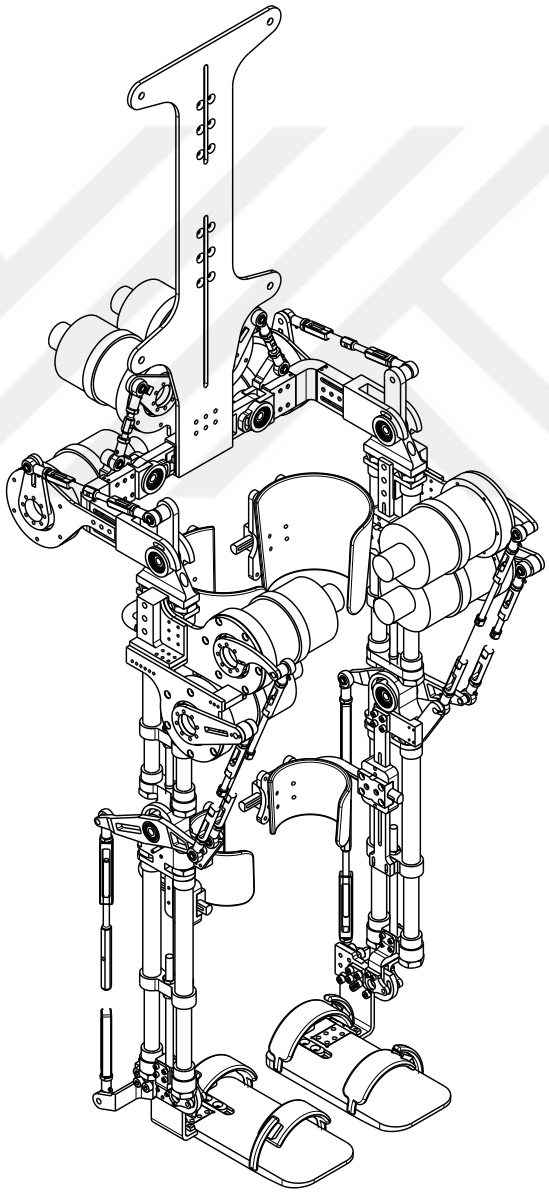

Figure 45: Final design version 1.1

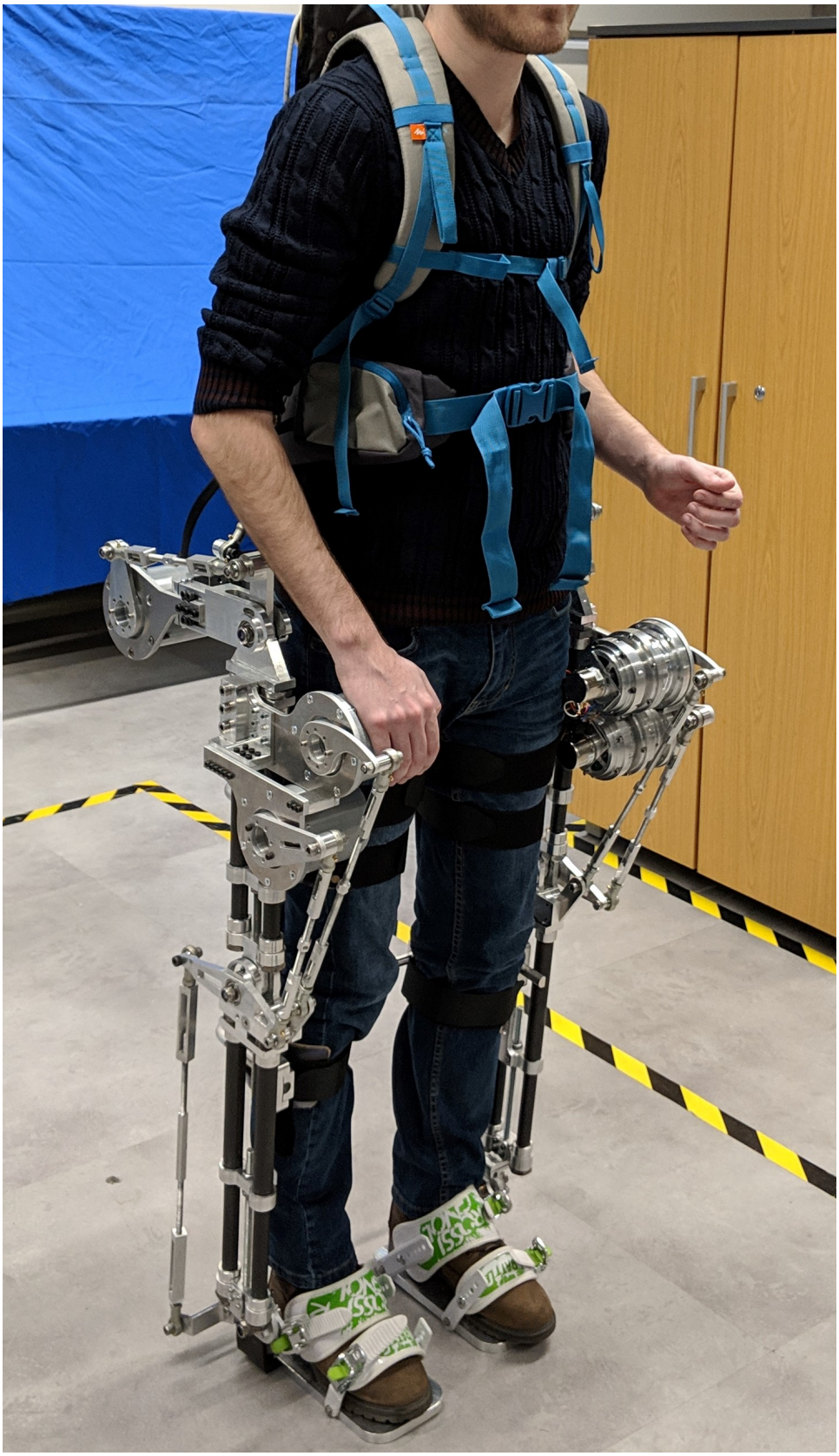

Figure 46: Manufactured version 1.1 with SEA, on a healthy male subject

APPENDIX C

SPRING-SUPPORTED PASSIVE ANKLE JOINT

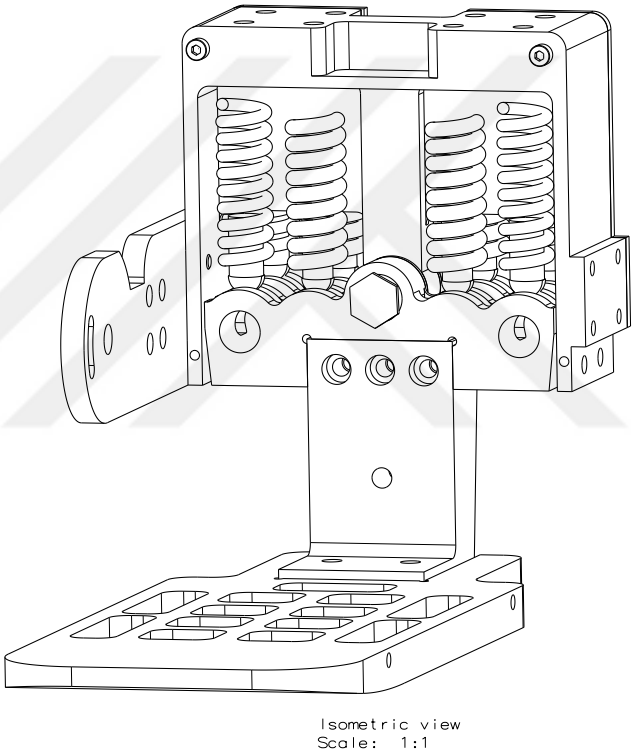

Figure 47: SEA timeline

Bibliography

[1] H. Vallery, R. Ekkelenkamp, H. Van Der Kooij, and M. Buss, "Passive and accurate torque control of series elastic actuators," in *IEEE/RSJ International Conference on Intelligent Robots and Systems (IROS)*, pp. 3534–3538, IEEE, 2007.

[2] "Spinal cord injury," *World Health Organization*.

[3] H. D. Celik, *Omurilik Felclilerinde Engellilik Durumunun ve Yasam Kalitesinin Degerlendirilmesi*. PhD thesis, Sisli Etfal Egitim ve Arastirma Hastanesi Fiziksel Tip ve Rehabilitasyon Klinigi, 2006.

[4] M. İ. Atagün, Ü. Altınok, Ö. D. Balaban, Z. Atagün, E. Yılmaz-Yalçınkaya, and K. Öneş, "Omurilik felçli hastalarda travma sonrası stres bozukluğu ve ilişkili faktörler.," *Klinik Psikiyatri Dergisi*, vol. 15, no. 2, 2012.

[5] M. Boakye, B. C. Leigh, and A. C. Skelly, "Quality of life in persons with spinal cord injury: comparisons with other populations," *Journal of Neurosurgery: Spine*, vol. 17, no. Suppl1, pp. 29–37, 2012.

[6] "World report on disability," *World report on Disability*, 2011.

[7] W. H. Organization, "Global disability action plan 2014-2021: Better ealth for all people with disability," 2015.

[8] A. Nene, H. Hermens, and G. Zilvold, "Paraplegic locomotion: A review," *Spinal cord*, vol. 34, no. 9, p. 507, 1996.

[9] T. Sumiya, K. Kawamura, A. Tokuhiro, H. Takechi, and H. Ogata, "A survey of wheelchair use by paraplegic individuals in japan. part 2: Prevalence of pressure sores," *Spinal cord*, vol. 35, no. 9, p. 595, 1997.

[10] D. L. O'Connor, J. M. Young, and M. J. Saul, "Living with paraplegia: Tensions and contradictions," *Health & Social Work*, vol. 29, no. 3, pp. 207–218, 2004.

[11] A. Esquenazi, S. Lee, A. T. Packel, and L. Braitman, "A randomized comparative study of manually assisted versus robotic-assisted body weight supported treadmill training in persons with a traumatic brain injury," *PM&R*, vol. 5, no. 4, pp. 280–290, 2013.

[12] J. C. Moreno, A. J. Del Ama, A. de Los Reyes-Guzmán, A. Gil-Agudo, R. Ceres, and J. L. Pons, "Neurorobotic and hybrid management of lower limb motor disorders: a review," *Medical & biological engineering & computing*, vol. 49, no. 10, p. 1119, 2011.

[13] J. Mehrholz, J. Kugler, and M. Pohl, "Locomotor training for walking after spinal cord injury," *Cochrane database of systematic reviews*, no. 11, 2012.

[14] C. Morawietz and F. Moffat, "Effects of locomotor training after incomplete spinal cord injury: a systematic review," *Archives of physical medicine and rehabilitation*, vol. 94, no. 11, pp. 2297–2308, 2013.

[15] G. Hardin, R. Benya, and J. Kasanin, "Methods and apparatus for supporting content distribution," May 7 2013. US Patent 8,438,603.

[16] A. Tsukahara, Y. Hasegawa, K. Eguchi, and Y. Sankai, "Restoration of gait for spinal cord injury patients using hal with intention estimator for preferable swing speed," *IEEE Transactions on Neural Systems and Rehabilitation Engineering*, vol. 23, no. 2, pp. 308–318, 2015.

[17] M. Talaty, A. Esquenazi, and J. E. Briceno, "Differentiating ability in users of the rewalk tm powered exoskeleton: An analysis of walking kinematics," in *in proc. of 2013 IEEE International Conference on Rehabilitation Robotics (ICORR)*, pp. 1–5, IEEE, 2013.

[18] A. J. Young and D. P. Ferris, "State of the art and future directions for lower limb robotic exoskeletons," *IEEE Transactions on Neural Systems and Rehabilitation Engineering*, vol. 25, no. 2, pp. 171–182, 2017.

[19] B. Ugurlu, H. Oshima, and T. Narikiyo, "Lower body exoskeleton-supported compliant bipedal walking for paraplegics: How to reduce upper body effort?," in *in proc. of 2014 IEEE International Conference on of Robotics and Automation (ICRA)*, pp. 1354–1360, IEEE, 2014.

[20] L. Brenner, "Exploring the psychosocial impact of ekso bionics technology," *Archives of Physical Medicine and Rehabilitation*, vol. 97, no. 10, p. e113, 2016.

[21] S. O. Schrade, K. Dätwyler, M. Stücheli, K. Studer, D.-A. Türk, M. Meboldt, R. Gassert, and O. Lambercy, "Development of varileg, an exoskeleton with variable stiffness actuation: first results and user evaluation from the cybathlon 2016," *Journal of neuroengineering and rehabilitation*, vol. 15, no. 1, p. 18, 2018.

[22] K. A. Strausser, T. A. Swift, A. B. Zoss, H. Kazerooni, and B. C. Bennett, "Mobile exoskeleton for spinal cord injury: Development and testing," in *ASME 2011 Dynamic Systems and Control Conference and Bath/ASME Symposium on Fluid Power and Motion Control*, pp. 419–425, American Society of Mechanical Engineers, 2011.

[23] "Berkeley robotics and human engineering laboratory."

[24] S. Kotov, V. Lijdvoy, A. Sekirin, K. Petrushanskaya, and E. Pismennaya, "The efficacy of the exoskeleton exoatlet to restore walking in patients with multiple sclerosis," *Zhurnal nevrologii i psikhiatrii imeni SS Korsakova*, vol. 117, no. 10. Vyp. 2, pp. 41–47, 2017.

[25] R. J. Farris, *Design of a powered lower-limb exoskeleton and control for gait assistance in paraplegics*. Vanderbilt University, 2012.

[26] P. D. Neuhaus, J. H. Noorden, T. J. Craig, T. Torres, J. Kirschbaum, and J. E. Pratt, "Design and evaluation of mina: A robotic orthosis for paraplegics," in *in proc. of 2011 IEEE International Conference on Rehabilitation Robotics (ICORR)*, pp. 1–8, 2011.

[27] A. Kozlowski, T. Bryce, and M. Dijkers, "Time and effort required by persons with spinal cord injury to learn to use a powered exoskeleton for assisted walking," *Topics in Spinal Cord injury rehabilitation*, vol. 21, no. 2, pp. 110–121, 2015.

[28] S. Lal, "Premature degenerative shoulder changes in spinal cord injury patients," *Spinal cord*, vol. 36, no. 3, p. 186, 1998.

[29] W. Pentland and L. Twomey, "Upper limb function in persons with long term paraplegia and implications for independence: Part i," *Spinal Cord*, vol. 32, no. 4, p. 211, 1994.

[30] L. L. Haubert, D. D. Gutierrez, C. J. Newsam, J. K. Gronley, S. J. Mulroy, and J. Perry, "A comparison of shoulder joint forces during ambulation with crutches versus a walker in persons with incomplete spinal cord injury," *Archives of physical medicine and rehabilitation*, vol. 87, no. 1, pp. 63–70, 2006.

[31] D. H. Nielsen, J. M. Harris, Y. M. Minton, N. S. Motley, J. L. Rowley, and C. T. Wadsworth, "Energy cost, exercise intensity, and gait efficiency of standard versus rocker-bottom axillary crutch walking," *Physical therapy*, vol. 70, no. 8, pp. 487–493, 1990.

[32] "Hank exoskeleton design."

[33] B. Ugurlu, C. Doppmann, M. Hamaya, P. Forni, T. Teramae, T. Noda, and J. Morimoto, "Variable ankle stiffness improves balance control: Experiments

on a bipedal exoskeleton," *IEEE/ASME Transactions on Mechatronics*, vol. 21, no. 1, pp. 79–87, 2016.

[34] T. Vouga, R. Baud, J. Fasola, M. Bouri, and H. Bleuler, "Twiice - a lightweight lower-limb exoskeleton for complete paraplegics," in *in proc. of 2017 International Conference on Rehabilitation Robotics (ICORR)*, pp. 1639–1645, 2017.

[35] S. Wang, L. Wang, C. Meijneke, E. Van Asseldonk, T. Hoellinger, G. Cheron, Y. Ivanenko, V. La Scaleia, F. Sylos-Labini, M. Molinari, *et al.*, "Design and control of the mindwalker exoskeleton," *IEEE Transactions on Neural Systems and Rehabilitation Engineering*, vol. 23, no. 2, pp. 277–286, 2015.

[36] G. Barbareschi, R. Richards, M. Thornton, T. Carlson, and C. Holloway, "Statically vs dynamically balanced gait: Analysis of a robotic exoskeleton compared with a human," in *in proc. of 37th Annual International Conference of the IEEE Engineering in Medicine and Biology Society (EMBC)*, pp. 6728–6731, 2015.

[37] A. Agrawal, O. Harib, A. Hereid, S. Finet, M. Masselin, L. Praly, A. D. Ames, K. Sreenath, and J. W. Grizzle, "First steps towards translating hzd control of bipedal robots to decentralized control of exoskeletons," *IEEE Access*, vol. 5, pp. 9919–9934, 2017.

[38] A. F. Soliman and B. Ugurlu, "A task prioritization-based inverse kinematics algorithm for an underactuated exoskeleton," in *Turkish Robotics Conference (ToRK)*, 2018.

[39] A. F. Soliman, P. Sendur, and B. Ugurlu, "3-d dynamic walking trajectory generation for a bipedal exoskeleton with underactuated legs: A proof of concept," in *IEEE International Conference on Rehabilitation Robotics (ICORR) 2019*, Submitted.

[40] E. Burdet, R. Osu, D. W. Franklin, T. E. Milner, and M. Kawato, "The central nervous system stabilizes unstable dynamics by learning optimal impedance," *Nature*, vol. 414, no. 6862, p. 446, 2001.

[41] M. Zinn, O. Khatib, B. Roth, and J. K. Salisbury, "Playing it safe [human-friendly robots]," *IEEE Robotics & Automation Magazine*, vol. 11, no. 2, pp. 12–21, 2004.

[42] A. De Santis, B. Siciliano, A. De Luca, and A. Bicchi, "An atlas of physical human–robot interaction," *Mechanism and Machine Theory*, vol. 43, no. 3, pp. 253–270, 2008.

[43] N. G. Tsagarakis, D. G. Caldwell, F. Negrello, W. Choi, L. Baccelliere, V. Loc, J. Noorden, L. Muratore, A. Margan, A. Cardellino, *et al.*, "Walk-man: A high-performance humanoid platform for realistic environments," *Journal of Field Robotics*, vol. 34, no. 7, pp. 1225–1259, 2017.

[44] R. Van Ham, T. G. Sugar, B. Vanderborght, K. W. Hollander, and D. Lefeber, "Compliant actuator designs," *IEEE Robotics & Automation Magazine*, vol. 16, no. 3, 2009.

[45] G. A. Pratt and M. M. Williamson, "Series elastic actuators," in *in proc. of 1995 IEEE/RSJ International Conference on Intelligent Robots and Systems 'Human Robot Interaction and Cooperative Robots'*, vol. 1, pp. 399–406, IEEE, 1995.

[46] D. Paluska and H. Herr, "The effect of series elasticity on actuator power and work output: Implications for robotic and prosthetic joint design," *Robotics and Autonomous Systems*, vol. 54, no. 8, pp. 667–673, 2006.

[47] J. Pratt, B. Krupp, and C. Morse, "Series elastic actuators for high fidelity force

control," *Industrial Robot: An International Journal*, vol. 29, no. 3, pp. 234–241, 2002.

[48] M. Hutter, C. D. Remy, M. A. Hoepflinger, and R. Siegwart, "High compliant series elastic actuation for the robotic leg scarl eth," in *Field Robotics*, pp. 507–514, World Scientific, 2012.

[49] C. Fitzgerald, "Developing baxter," in *in proc. of 2013 IEEE International Conference on Technologies for Practical Robot Applications (TePRA)*, pp. 1–6, IEEE, 2013.

[50] J. F. Veneman, R. Ekkelenkamp, R. Kruidhof, F. C. van der Helm, and H. van der Kooij, "A series elastic-and bowden-cable-based actuation system for use as torque actuator in exoskeleton-type robots," *The International Journal of Robotics Research*, vol. 25, no. 3, pp. 261–281, 2006.

[51] R. Van Ham, B. Vanderborght, M. Van Damme, B. Verrelst, and D. Lefeber, "Maccepa, the mechanically adjustable compliance and controllable equilibrium position actuator: Design and implementation in a biped robot," *Robotics and Autonomous Systems*, vol. 55, no. 10, pp. 761–768, 2007.

[52] N. Paine, S. Oh, and L. Sentis, "Design and control considerations for high-performance series elastic actuators," *IEEE/ASME Transactions on Mechatronics*, vol. 19, no. 3, pp. 1080–1091, 2014.

[53] E. Sariyildiz, G. Chen, and H. Yu, "An acceleration-based robust motion controller design for a novel series elastic actuator," *IEEE Transactions on Industrial Electronics*, vol. 63, no. 3, pp. 1900–1910, 2016.

[54] E. J. Rouse, L. M. Mooney, E. C. Martinez-Villalpando, and H. M. Herr, "Clutchable series-elastic actuator: Design of a robotic knee prosthesis for minimum energy consumption," pp. 1–6, 2013.

[55] N. G. Tsagarakis, S. Morfey, G. M. Cerda, L. Zhibin, and D. G. Caldwell, "Compliant humanoid coman: Optimal joint stiffness tuning for modal frequency control," in *in proc. of 2013 IEEE International Conference on Robotics and Automation (ICRA)*, pp. 673–678, IEEE, 2013.

[56] J. N. Yun, J. Su, Y. I. Kim, and Y. C. Kim, "Robust disturbance observer for two-inertia system," *IEEE Transactions on Industrial Electronics*, vol. 60, no. 7, pp. 2700–2710, 2013.

[57] P. Kormushev, B. Ugurlu, S. Calinon, N. G. Tsagarakis, and D. G. Caldwell, "Bipedal walking energy minimization by reinforcement learning with evolving policy parameterization," in *in proc. of 2011 IEEE/RSJ International Conference on Intelligent Robots and Systems (IROS)*, pp. 318–324, IEEE, 2011.

[58] F. Negrello, M. Garabini, M. G. Catalano, J. Malzahn, D. G. Caldwell, A. Bicchi, and N. G. Tsagarakis, "A modular compliant actuator for emerging high performance and fall-resilient humanoids," in *2015 IEEE-RAS 15th International Conference on Humanoid Robots (Humanoids)*, pp. 414–420, Nov 2015.

[59] N. Paine, J. S. Mehling, J. Holley, N. A. Radford, G. Johnson, C.-L. Fok, and L. Sentis, "Actuator control for the nasa-jsc valkyrie humanoid robot: A decoupled dynamics approach for torque control of series elastic robots," *Journal of Field Robotics*, vol. 32, no. 3, pp. 378–396, 2015.

[60] A. Parmiggiani, G. Metta, and N. Tsagarakis, "The mechatronic design of the new legs of the icub robot," in *2012 12th IEEE-RAS International Conference on Humanoid Robots (Humanoids 2012)*, pp. 481–486, Nov 2012.

[61] D. Accoto, G. Carpino, F. Sergi, N. L. Tagliamonte, L. Zollo, and E. Guglielmelli, "Design and characterization of a novel high-power series elastic

actuator for a lower limb robotic orthosis," *International Journal of Advanced Robotic Systems*, vol. 10, no. 10, p. 359, 2013.

[62] N. Paine and L. Sentis, "Design and comparative analysis of a retrofitted liquid cooling system for high-power actuators," in *Actuators*, vol. 4, pp. 182–202, Multidisciplinary Digital Publishing Institute, 2015.

[63] D. Kim, O. Campbell, J. Ahn, L. Sentis, and N. Paine, "Investigations of viscoelastic liquid cooled actuators applied for dynamic motion control of legged systems," in *in proc. of 2017 IEEE-RAS 17th International Conference on Humanoid Robotics (Humanoids)*, pp. 710–717, IEEE, 2017.

[64] J. T. Kendrick, *Design of High-Performance, Dual-Motor Liquid-Cooled, Linear Series Elastic Actuators for a Self-Balancing Exoskeleton*. PhD thesis, Virginia Tech, 2018.

[65] J. F. Veneman, R. Kruidhof, E. E. Hekman, R. Ekkelenkamp, E. H. Van Asseldonk, and H. Van Der Kooij, "Design and evaluation of the lopes exoskeleton robot for interactive gait rehabilitation," *IEEE Transactions on Neural Systems and Rehabilitation Engineering*, vol. 15, no. 3, pp. 379–386, 2007.

[66] M. K. Shepherd and E. J. Rouse, "Design and validation of a torque-controllable knee exoskeleton for sit-to-stand assistance," *IEEE/ASME Transactions on Mechatronics*, vol. 22, no. 4, pp. 1695–1704, 2017.

[67] T. Zhang, M. Tran, and H. Huang, "Design and experimental verification of hip exoskeleton with balance capacities for walking assistance," *IEEE/ASME Transactions on Mechatronics*, vol. 23, no. 1, pp. 274–285, 2018.

[68] S.-S. Yoon, S. Kang, S.-k. Yun, S.-J. Kim, Y.-H. Kim, and M. Kim, "Safe arm design with mr-based passive compliant joints and viscoelastic covering

for service robot applications," *Journal of mechanical science and technology*, vol. 19, no. 10, pp. 1835–1845, 2005.

[69] H.-C. Hsieh, D.-F. Chen, L. Chien, and C.-C. Lan, "Design of a parallel actuated exoskeleton for adaptive and safe robotic shoulder rehabilitation," *IEEE/ASME Transaction on Mechatronics*, vol. 22, no. 5, pp. 2034–2045, 2017.

[70] N. Kashiri, J. Malzahn, and N. G. Tsagarakis, "On the sensor design of torque controlled actuators: A comparison study of strain gauge and encoder-based principles," *IEEE Robotics and Automation Letters*, vol. 2, no. 2, pp. 1186–1194, 2017.

[71] C. Lagoda, A. C. Schouten, A. H. A. Stienen, E. E. G. Hekman, and H. van der Kooij, "Design of an electric series elastic actuated joint for robotic gait rehabilitation training," in *2010 3rd IEEE RAS EMBS International Conference on Biomedical Robotics and Biomechatronics*, pp. 21–26, Sept 2010.

[72] N. G. Tsagarakis, M. Laffranchi, B. Vanderborght, and D. G. Caldwell, "A compact soft actuator unit for small scale human friendly robots," in *2009 IEEE International Conference on Robotics and Automation*, pp. 4356–4362, May 2009.

[73] F. Negrello, M. G. Catalano, M. Garabini, M. Poggiani, D. G. Caldwell, N. G. Tsagarakis, and A. Bicchi, "Design and characterization of a novel high-compliance spring for robots with soft joints," in *in proc. of 2017 IEEE International Conference on Advanced Intelligent Mechatronics (AIM)*, pp. 271–278, July 2017.

[74] W. F. Hosford and R. M. Caddell, *Metal forming: mechanics and metallurgy*. Cambridge University Press, 2007.

[75] M. C. Yildirim, P. Sendur, O. Bilgin, B. Gulek, G. G. Yapici, and B. Ugurlu, "An integrated design approach for a series elastic actuator: Stiffness formulation, fatigue analysis, thermal management," in *in proc. of 2017 IEEE-RAS 17th International Conference on Humanoid Robotics (Humanoids)*, pp. 384–389, IEEE, 2017.

[76] M. C. Yildirim, A. T. Kansizoglu, P. Sendur, and B. Ugurlu, "High power series elastic actuator development for torque-controlled exoskeletons," in *International Symposium on Wearable Robotics*, pp. 70–74, Springer, 2018.

[77] M. Hutter, C. Gehring, D. Jud, A. Lauber, C. D. Bellicoso, V. Tsounis, J. Hwangbo, K. Bodie, P. Fankhauser, M. Bloesch, *et al.*, "Anymal-a highly mobile and dynamic quadrupedal robot," in *2016 IEEE/RSJ International Conference on Intelligent Robots and Systems (IROS)*, pp. 38–44, IEEE, 2016.

[78] A. T. Kansizoglu, E. Sariyildiz, and B. Ugurlu, "A comparison study on observer-based force control of series elastic actuators," in *in proc. of 2018 IEEE 15th International Workshop on Advanced Motion Control (AMC)*, pp. 411–416, IEEE, 2018.

[79] S. Wang, C. Meijneke, and H. van der Kooij, "Modeling, design, and optimization of mindwalker series elastic joint," in *in proc. of 2013 IEEE International Conference on Rehabilitation Robotics (ICORR)*, pp. 1–8, IEEE, 2013.

[80] R. Oskouei and R. Ibrahim, "The effect of a heat treatment on improving the fatigue properties of aluminium alloy 7075-t6 coated with tin by pvd," *Procedia Engineering*, vol. 10, pp. 1936–1942, 2011.

[81] M. Miner, "Cumulative damage in fatigue journal of applied mechanics 12 (1945) no. 3, pp," *A159-A164*, 1945.

[82] Y. Ito, S. Nozawa, J. Urata, T. Nakaoka, K. Kobayashi, Y. Nakanishi, K. Okada, and M. Inaba, "Development and verification of life-size humanoid with high-output actuation system," in *in proc. of 2014 IEEE International Conference on Robotics and Automation (ICRA)*, pp. 3433–3438, IEEE, 2014.

[83] J. Garg, M. Arik, S. Weaver, and S. Saddoughi, "Micro fluidic jets for thermal management of electronics," in *ASME 2004 Heat Transfer/Fluids Engineering Summer Conference*, pp. 647–654, American Society of Mechanical Engineers, 2004.

[84] G. A. Pratt, M. M. Williamson, P. Dillworth, J. Pratt, and A. Wright, "Stiffness isn't everything," in *Experimental Robotics IV*, pp. 253–262, Springer, 1997.

[85] D. W. Robinson, *Design and analysis of series elasticity in closed-loop actuator force control*. PhD thesis, Massachusetts Institute of Technology, 2000.

[86] G. Wyeth, "Control issues for velocity sourced series elastic actuators," in *in proc. of the Australasian Conference on Robotics and Automation 2006*, Australian Robotics and Automation Association Inc, 2006.

[87] V. Bartenbach, M. Gort, and R. Riener, "Concept and design of a modular lower limb exoskeleton," in *in proc. of 2016 6th IEEE International Conference on Biomedical Robotics and Biomechatronics (BioRob)*, pp. 649–654, IEEE, 2016.

[88] J. E. Pratt, B. T. Krupp, C. J. Morse, and S. H. Collins, "The roboknee: an exoskeleton for enhancing strength and endurance during walking," in *in proc. of 2004 IEEE International Conference on Robotics and Automation*, vol. 3, pp. 2430–2435, IEEE, 2004.

[89] B. Ugurlu, J. A. Saglia, N. G. Tsagarakis, S. Morfey, and D. G. Caldwell,

"Bipedal hopping pattern generation for passively compliant humanoids: Exploiting the resonance," *IEEE Transactions on Industrial Electronics*, vol. 61, no. 10, pp. 5431–5443, 2014.

[90] J. Zhang, P. Fiers, K. A. Witte, R. W. Jackson, K. L. Poggensee, C. G. Atkeson, and S. H. Collins, "Human-in-the-loop optimization of exoskeleton assistance during walking," *Science*, vol. 356, no. 6344, pp. 1280–1284, 2017.

[91] M. Vukobratović and B. Borovac, "Zero-moment pointthirty five years of its life," *International Journal of Humanoid Robotics*, vol. 1, no. 01, pp. 157–173, 2004.

[92] P. De Leva, "Adjustments to zatsiorsky-seluyanov's segment inertia parameters," *Journal of Biomechanics*, vol. 29, no. 9, pp. 1223–1230, 1996.

[93] R. Dumas, L. Cheze, and J.-P. Verriest, "Adjustments to mcconville et al. and young et al. body segment inertial parameters," *Journal of Biomechanics*, vol. 40, no. 3, pp. 543–553, 2007.

[94] A. Leardini, J. OConnor, F. Catani, and S. Giannini, "Kinematics of the human ankle complex in passive flexion; a single degree of freedom system," *Journal of Biomechanics*, vol. 32, no. 2, pp. 111–118, 1999.

[95] D. A. Winter, A. E. Patla, S. Rietdyk, and M. G. Ishac, "Ankle muscle stiffness in the control of balance during quiet standing," *Journal of Neurophysiology*, vol. 85, no. 6, pp. 2630–2633, 2001.

[96] K. Rodriguez, J. de Groot, F. Baas, M. Stijntjes, F. van der Helm, H. van der Kooijl, and W. Mugge, "Passive ankle joint stiffness compensation by a novel ankle-foot-orthosis," in *2018 7th IEEE International Conference on Biomedical Robotics and Biomechatronics (Biorob)*, pp. 517–522, IEEE, 2018.

[97] S. Kajita, F. Kanehiro, K. Kaneko, K. Yokoi, and H. Hirukawa, "The 3d linear inverted pendulum mode: A simple modeling for a biped walking pattern generation," in *in proc. of 2001 IEEE/RSJ International Conference on Intelligent Robots and Systems*, vol. 1, pp. 239–246, IEEE, 2001.

[98] A. K. Sanyal and A. Goswami, "Dynamics and balance control of the reaction mass pendulum: A three-dimensional multibody pendulum with variable body inertia," *Journal of Dynamic Systems, Measurement, and Control*, vol. 136, no. 2, p. 021002, 2014.

[99] B. Ugurlu and A. Kawamura, "Bipedal trajectory generation based on combining inertial forces and intrinsic angular momentum rate changes: Eulerian zmp resolution," *IEEE Transactions on Robotics*, vol. 28, no. 6, pp. 1406–1415, 2012.

[100] X. Da, O. Harib, R. Hartley, B. Griffin, and J. W. Grizzle, "From 2d design of underactuated bipedal gaits to 3d implementation: Walking with speed tracking," *IEEE Access*, vol. 4, pp. 3469–3478, 2016.

[101] "Cassie designed to be agile and efficient."

[102] A. Hereid, O. Harib, R. Hartley, Y. Gong, and J. W. Grizzle, "Rapid bipedal gait design using c-frost with illustration on a cassie-series robot," *arXiv preprint arXiv:1807.06614*, 2018.

[103] N. Tsagarakis, F. Negrello, M. Garabini, W. Choi, L. Baccelliere, V. Loc, J. Noorden, M. Catalano, M. Ferrati, L. Muratore, *et al.*, "Walk-man humanoid platform," in *The DARPA Robotics Challenge Finals: Humanoid Robots To The Rescue*, pp. 495–548, Springer, 2018.

[104] M. Hora, L. Soumar, H. Pontzer, and V. Sládek, "Body size and lower limb posture during walking in humans," *PloS one*, vol. 12, no. 2, p. e0172112, 2017.

[105] R. G. Budynas, J. K. Nisbett, *et al.*, *Shigley's mechanical engineering design*, vol. 8. McGraw-Hill New York, 2008.

[106] V. Bartenbach, D. Wyss, D. Seuret, and R. Riener, "A lower limb exoskeleton research platform to investigate human-robot interaction," in *in proc. of 2015 IEEE International Conference on Rehabilitation Robotics (ICORR)*, pp. 600–605, IEEE, 2015.

[107] Y. Liao, Z. Zhou, and Q. Wang, "Biokex: A bionic knee exoskeleton with proxy-based sliding mode control," in *in proc. of 2015 IEEE International Conference on Industrial Technology (ICIT)*, pp. 125–130, IEEE, 2015.

[108] Z. F. Lerner, D. L. Damiano, H.-S. Park, A. J. Gravunder, and T. C. Bulea, "A robotic exoskeleton for treatment of crouch gait in children with cerebral palsy: Design and initial application," *IEEE Transactions on Neural Systems and Rehabilitation Engineering*, vol. 25, no. 6, pp. 650–659, 2017.

[109] B. N. Fournier, E. D. Lemaire, A. J. Smith, and M. Doumit, "Modeling and simulation of a lower extremity powered exoskeleton," *IEEE Transactions on Neural Systems and Rehabilitation Engineering*, vol. 26, no. 8, pp. 1596–1603, 2018.

[110] J. Y. Lee, *A lower-limb exoskeleton emulator to be employed in estimation of hip impedance in normal gait.* PhD thesis, Colorado School of Mines. Arthur Lakes Library, 2017.

VITA

Mehmet Can YILDIRIM was born in 1993 in Merzifon/TURKEY. He graduated from TEV İnanç Türkeş High School for Gifted Students, before starting his Bachelor's Degree studies at Özyeğin University Mechanical Engineering Department in 2012. He worked as an undergraduate research student for 3.5 years at Özyeğin University Robotics Laboratory, under the supervision of Asst. Prof. Özkan Bebek. He also acted as the American Society of Mechanical Engineers (ASME) Student Regional Chair for Europe and Northern Asia between August 2015 to September 2016. After receiving his BSc degree in 2016, he started his master studies in the same institution. Between September 2016 to January 2019, he worked both as a research assistant and the laboratory leader in Özyeğin University Biomechatronics Laboratory, under the supervision of Asst. Prof. Barkan Ugurlu. Mr. YILDIRIM is the recipient of Best Research Assistant Award 2018 which is granted by Özyeğin University School of Engineering.